Unveiling the cell biology of hippocampal neurons with dendritic axon origin

Yuhao Han[1, 2, 3, 4], Roland Thuenauer[5, 6, 8], Kay Grünewald[3, 4, 7]*, Marina Mikhaylova[1 ,2, 9]*

[1]AG Optobiology, Institute of Biology, Humboldt Universität zu Berlin, Berlin, 10115 Germany

[2] Guest Group "Neuronal Protein Transport", Centre for Molecular Neurobiology, University Medical Center Hamburg-Eppendorf, Hamburg, 20251 Germany

[3] Centre for Structural Systems Biology, Hamburg, 22607 Germany

[4] Structural Cell Biology of Viruses, Leibniz Institute of Virology (LIV), Hamburg, 20251 Germany

[5]Advanced Light and Fluorescence Microscopy (ALFM) Facility, Centre for Structural Systems Biology, Hamburg, 22607 Germany

[6] Technology Platform Light Microscopy, University of Hamburg, Hamburg, Germany

[7] Department of Chemistry, University of Hamburg, Hamburg, 20146 Germany

[8]Technology Platform Microscopy and Image Analysis (TP MIA), Leibniz Institute of Virology (LIV), Hamburg, Germany

* Correspondence: kay.gruenewald@cssb-hamburg.de and marina.mikhaylova@hu-berlin.de

[9] Lead contact: marina.mikhaylova@hu-berlin.de

Summary

In axon-carrying-dendrite (AcD) neurons, the axon emanates from a basal dendrite, instead of the soma, to create a privileged route for action potential generation at the axon initial segment (AIS). However, it is unclear how such unusual morphology is established and whether the structural and functional integrity of the AIS in AcD neurons is preserved. Here, we show that the AcD neurons follow an intrinsically encoded developmental program where a single precursor neurite first gives rise to the axon and then to the AcD. The AIS possesses a similar cytoskeletal architecture as the canonical AIS that stems from the soma, and similarly functions as a trafficking barrier to retain axon-specific molecular composition. However, unlike soma-derived AIS, the AIS of AcD neurons does not undergo homeostatic-plasticity, contains less cisternal organelles and receives fewer inhibitory inputs. These distinct features of the AIS could account for higher intrinsic excitability of AcD neurons.

Highlights

- The development of AcD neurons is intrinsically driven and does not depend on neuronal connectivity
- AcD neurons generate the axon and AcD from the same precursor neurite
- The stem dendrite of an AcD neuron displays axon-like microtubule organization
- Similar to the AIS emerging from the soma, the AIS of AcD neurons can selectively filter dendritic cargo
- The AIS of AcD neurons does not undergo homeostatic plasticity and receives fewer inhibitory inputs

Keywords

Axon-carrying dendrite neurons, axon initial segment (AIS), cytoskeleton, AIS plasticity, cisternal organelle

Introduction

Principal excitatory neurons comprise three functional domains: a soma, multiple highly branched dendrites and a single axon. Canonically, the axon of a principal neuron emerges directly from the soma. An important function of the axon is to communicate with downstream targets by transmitting inputs that have been received at the dendrites and integrated at the soma in the form of action potentials (APs). Axon formation is the initial step in development of neuronal polarity.[1] After mitotic phase, the spherical-shaped neurons first generate a pool of nascent neurites and then specify a single precursor neurite to become an axon.[2,3] Once the axon is properly established, the remaining neurites begin to differentiate into dendrites and synaptic connections are eventually formed.[2,3] Such development program is mostly genetically encoded in neurons and can be reproduced in dissociated cell cultures.[1] However, the timing, topology of subcellular domains, connectivity, and certain other specific aspects of neuron development can vary between cell types. This variation may be attributed to the distinct microenvironments formed by *in vivo* guidance molecules.[1,3]

The axon of a principal neuron contains several distinct cellular features that are essential for its functions. For example, the fast growing microtubule (MT) plus ends in the axon are uniformly arranged towards the distal tip, whereas in the dendrites are bi-directionally oriented.[4,5] The stability of axonal MTs is also enhanced by employing specific ratio of post-translational modifications (PTMs).[4,5] This unique axonal MT organisation has been shown to promote targeted delivery of vesicles containing axon specific proteins and lipids which is driven by kinesin motor proteins.[6–8] The axon initial segment (AIS) is another important structure covering the proximal part of the axon and extending about 20-60 µm towards the distal end. The hallmarks of the AIS include: the patch-like filamentous actin (F-actin) networks[9–12]; the periodical membrane cytoskeleton (MPS) consisting of F-actin rings separated by AIS specific scaffolding proteins ankyrin-G (AnkG) and spectrins[10–15]; the MT fascicles bundled by AIS specific MT associated protein (MAP) TRIM46[16]; the voltage gated ion channels (VGICs), such as sodium channels , enriched on the plasma membrane[17], and the cisternal organelles (COs),

which is a stack of endoplasmic reticulum (ER) membrane linked together by actin binding protein synaptopodin (Synpo).[18–20] Together, this sophisticated cellular organisation makes the AIS a critical structure that not only acts as a molecular fence to filter out somatodendritic proteins[9–11], but also initiate APs along the axon and regulate neuronal excitability and homeostasis.[13,21–23] It has been shown that the AIS of excitatory neurons undergo structural remodelling to compensate for high neuronal activity, a process known as AIS plasticity.[22,23] Furthermore, the AIS of excitatory neurons is innervated by inhibitory synapses for fine-tuning of excitability during network activities[24]. Therefore, the structural and functional integrity of the AIS is extremely important for proper neuronal functions.

Different from canonical morphology, the axon of some neurons can also emanate from a dendrite. Already in 1899, Ramon Cajal observed neurons with the axon emerging from a dendrite in unipolar neurons of invertebrate abdominal ganglia.[25] Later, neurons with an axon emerging from a basal dendrite have been discovered in the neocortex and hippocampus of mammals, including human.[26–28] This type of neurons is referred to as axon-carrying dendrite (AcD) neurons[26]. A typical feature of AcD neuron is that the axon and the AcD branch out from a common dendritic root, called stem dendrite.[26–28] In rodent hippocampus, AcD neurons were found to be primarily distributed at the central part of the CA1 region, where they represent over 50% of the entire excitatory neuron population.[26] Electrophysiological experiments suggested that the AcD is intrinsically more excitable than regular somatic dendrites.[26] Since the AIS is located next to the AcD, synaptic inputs from the AcD can bypass somatic integration, and directly flow into the axon to trigger AP at the AIS.[26] This AcD-to-AIS paradigm of AP initiation allows the AcD neurons to evade global peri-somatic inhibition, and therefore being selectively activated during sharp-wave ripples, a process associated with memory consolidation.[28] Collectively, these findings revealed that the dendritic AIS origin has a substantial impact on the electrical behaviour of hippocampal excitatory neurons. Despite a detailed physiological and functional characterisation of AcD neurons, several cell biological questions have remained open. For instance, is the development of AcD neurons dependent on neuronal connectivity and guidance cues or that AcD neuron differentiation is intrinsically encoded? How do AcD neurons develop the axon and AIS from a

52 dendrite? What is the cytoskeletal organisation of AcD neurons, especially at the AIS, and is it different
53 to canonical AIS emerging directly from the soma? Are the AIS functions affected by the localisation at
54 a dendrite? In this study, we aim to provide a more comprehensive cell biological picture of
55 hippocampal AcD neurons by addressing these questions.

56 **Results**

57 **The AcD neurons follow intrinsically encoded developmental program and differentiate the**
58 **axon and AcD from the same precursor neurite**

59 To investigate whether the differentiation of hippocampal neurons into AcD type is intrinsically or
60 extrinsically driven, we used dissociated hippocampal primary cultures because they lack the
61 microenvironments that guide neuron development *in vivo*. Immunofluorescent labelling of the AIS
62 marker AnkG and of the somatodendritic marker MAP2 clearly showed that, in a subset of neurons,
63 the AIS is branched out from a dendrite and located further away from the soma (Figure 1A), indicating
64 that hippocampal neurons do differentiate into AcD type in dissociated cultures. Already at 3 days in
65 vitro (DIV), the AnkG fluorescent signal began to accumulate at the proximal axon of AcD neurons
66 (Figure 1A), and the signal appears to be more continuous and evident in AcD neurons fixed at later
67 time point (DIV5, 7 and 12), when the AIS is more mature (Figure 1A). The same time line of AIS
68 formation was also observed in nonAcD neurons (Figure 1A), which is consistent with a previous
69 study.[29] These results suggest that the development of AcD neurons is indeed an intrinsically driven
70 process, and that the dendritic axon origin has no impact on the timing of AIS assembly.

71 For further investigation, we classified hippocampal neurons into AcD and nonAcD categories based
72 on previously published standards[26–28], and quantified the amount of AcD neurons in dissociated
73 cultures at DIV5 and DIV7, at which neuronal polarity has been established. The axon distance from
74 the soma was the key factor for AcD neuron classification (Figure 1B; Figure S1D; see STAR methods
75 for details). We classified neurons with an axon distance longer than 3 µm as AcD neurons. Otherwise,
76 neurons were considered as nonAcD. Quantification showed that AcD neurons make up 15-20% of the
77 entire population at both time points (Figure 1C), indicating that dissociated cultures can be a good
78 model system to investigate cell biology of AcD neurons.

79 The canonical developmental process of nonAcD neurons *in vitro* is defined into five stages.[2] After
80 surface attachment, neurons begin with generating a pool of nascent neurites and then specifying a
81 single precursor neurite as the axon (stage 1-3; DIV0-3) (Figure 1D; Video S1). Subsequently, the rest
82 of the neurites begin to differentiate into dendrites (stage 4; DIV4-7; Figure 1D; Video S1), followed by
83 establishing synapses (stage 5; after DIV7). We therefore asked whether AcD neurons keep the same
84 developmental sequence, given their atypical axon origin. Indeed, 5 days of continues time lapse
85 imaging with post-labelling of the AIS to categorise neurons revealed that AcD neurons also first grow
86 an axon from a precursor neurite and then establish dendrites (Figure 1D; Figure S1A; Video S2).
87 However, during early stages of development (DIV1-2), a collateral neurite was generated from the
88 proximal region of the precursor neurite that is designated as the axon (Figure 1D; Figure S1A; Video
89 S2). This collateral underwent several rounds of elongation and retraction while the precursor neurite
90 kept developing as the axon (Figure 1D; Figure S1A; Video S2). Eventually, once the axon was defined,
91 the collateral started to mature as the AcD and the former proximal region of the precursor neurite
92 was transformed into the stem dendrite (Figure 1D; Figure S1A; Video S2). Quantitative analysis
93 showed that about 80% of the AcD neurons generate collateral at the proximal region of the precursor
94 neurite (Figure 1E), and the average time point of collateral formation is at 39 hours (DIV1.5) post
95 plating (Figure 1F). About 20% of the AcD neurons developed axon and AcD via bifurcation of the
96 precursor neurite growth cone (Figure 1E; Figure S1B; Video S3). Among the 80% of AcD neurons that
97 formed collateral, majority of the population (70%) designated the precursor neurite as the axon and
98 grew the collateral as AcD (Figure 1G). Only a smaller population (30%) of neurons turned the precursor
99 neurite into the AcD, and a collateral that emerged next to the precursor neurite growth cone
100 developed into the axon (Figure 1G; Figure S1A; Video S4). We also assessed the collateral genesis at
101 the proximal region of the axon precursor neurite in nonAcD neurons. We found only 30% of nonAcD
102 neurons formed collaterals at DIV1 (Figure 1H), and these collaterals completely retracted at DIV4
103 (Figure S1C), meaning that the precursor neurite of AcD neurons has higher tendency to generate
104 collateral during development. Together, these findings suggest that the AcD and axon of AcD neurons

105 are differentiated from a common precursor neurite. This neurite is primarily identified as the axon
106 and the AcD is established mainly via collateralization post axon formation (Figure 1I). Although,
107 multiple alternative strategies do exist during AcD neuron development which is similar to what has
108 been shown for nonAcD neurons *in vitro*.[2]

109 **The stem dendrite of AcD neurons has axon-like microtubule organisation**

110 The different orientation of MTs between axon and dendrites in neurons is important for directional
111 transport of axonal and dendritic cargoes.[4–6,30] We therefore wondered if the MT orientation in AcD
112 neurons differs from nonAcD neurons, especially at the region of the stem dendrite, axon and AcD. To
113 track MT orientations, we overexpressed MT plus end binding protein-3 tagged with Tdtomato (EB3-
114 Tdtomato) in DIV14 dissociated neurons. For axon identification, we labelled the AIS with a
115 fluorescently conjugated antibody against the extracellular domain of the AIS enriched
116 transmembrane protein neurofascin (anti-NF-CF640R) in live cells (Figure S1E). We found that the AIS,
117 axon and regular somatic dendrites of AcD neurons display similar MT orientations as nonAcD neurons.
118 As indicated by EB3-Tdtomato trajectories, in both AcD and nonAcD neurons, MT plus ends in the AIS
119 and axon are uniformly oriented towards the distal tip but are anti-parallel in the regular somatic
120 dendrites (Figure 2A and 2C; Video S5 - S7). In AcD neurons, we also observed mixed directions of EB3-
121 Tdtomato trajectories in the AcD (Figure 2B and 2C; Video S5), suggesting that the AcD has a typical
122 dendritic MT organisation. By stark contrast, we found that in the stem dendrite of AcD neurons, nearly
123 90% of the EB3-Tdtomato trajectories showed a unidirectional movement either towards the axon or
124 the AcD (Figure 2B and 2C; Video S5). This unidirectional plus end-out MT orientation highly resembles
125 that in the axon.

126 Previous studies have demonstrated that stable acetylated MTs are more abundant in the axon than
127 in the dendrites[5], and the presence of acetylated MTs is instructive for protein delivery into the axon
128 via kinesin-1[7,31], a member of kinesin motor protein family. To visualise different MT populations, we
129 performed gated-stimulation emission depletion (gSTED) super-resolution imaging which revealed the

130 presence of acetylated MTs at the stem dendrite of AcD neurons (Figure 2D). These acetylated MTs
131 are located in the middle of the stem dendrite and surrounded by dynamic tyrosinated MTs (Figure 2D
132 and 2E), which is very similar to axons of nonAcD neurons.[32] Moreover, we found that acetylated MTs
133 extend from the stem dendrite directly into the AIS, while they occur less in the AcD (Figure 2D). Since
134 our developmental data showed that the stem dendrite mostly derives from the axon precursor
135 neurite, these results indicate that the stem dendrite of AcD neurons inherits axonal MT organisation.

136 **The AIS of AcD neurons has the same F-actin organisation as in nonAcD neurons but contains**
137 **less cisternal organelles**

138 In nonAcD neurons, the AIS is supported by F-actin-rich structures, including the MPS and the F-actin
139 patches.[9–12,14,15] However, it has not been shown whether the AIS of AcD neurons has a similar actin
140 organisation. We therefore labelled F-actin in dissociated AcD neurons with phalloidin-Atto647N and
141 performed gSTED imaging to visualise the nanoscale architecture of F-actin. We found that the F-actin
142 at the AIS of AcD neurons also formed individual patches and ring-like structures (Figure 3A). The F-
143 actin rings were periodically arranged with a spacing of about 190 nm (Figure 3B), indicating that the
144 F-actin at the AIS of AcD neurons has similar nanostructure to nonAcD neurons. Previous work has
145 shown that in hippocampal excitatory neurons, the axonal F-actin patches colocalise with COs[20], and
146 this colocalization is mediated by the actin binding protein synaptopodin.[18,19,33] Interestingly, our
147 quantification showed a relatively lower number of synaptopodin puncta at the AIS of AcD neurons
148 than nonAcD neurons (Figure 3C and 3D), indicating that the amount of COs is reduced at the AIS of
149 AcD neurons.

150 **The AIS of AcD neurons regulates neuronal polarity by selective permissiveness for axonal**
151 **cargoes**

152 The AIS helps the axon to retain distinct protein composition by selectively blocking MT based
153 trafficking of dendritic cargoes.[13,21] This selectivity depends on F-actin structures.[9–12] Our data showed
154 that there is no difference on F-actin nanostructure between the AIS of AcD and nonAcD neurons,
155 suggesting that the cargo selectivity of the AIS may also remain unchanged in AcD neurons. To
156 experimentally assess this, we used two well established markers, Ras-related protein Rab3A, which
157 associates with pre-synaptic vesicles, and transferrin receptors (TfRs) as representative axonal and
158 dendritic cargoes, respectively.[34,35] We infected neurons with recombinant adeno-associated virus
159 (rAAV) expressing Rab3A tagged with EGFP (EGFP-Rab3A) to visualise axonal cargoes. The AIS was live
160 labelled with anti-NF-CF640R antibody (Figure S1E). To reduce background signals of EGFP-Rab3A, we
161 photobleached the fluorescent signal of EGFP-Rab3A vesicles residing at the imaging area and
162 recorded newly delivered EGFP-Rab3A vesicles. Kymographs of time lapse recordings revealed that
163 EGFP-Rab3A vesicles in AcD neurons specifically recognise the axon location, then travel through the
164 stem dendrite region into the AIS and the axon (Figure 4A-4C; Video S8). For dendritic cargoes, we live
165 labelled endogenous TfRs of neurons with the fluorescently conjugated ligand Transferrin-Alexa568.
166 We found that TfR vesicles were halted at the AIS and were mostly travelling within the dendritic region
167 of AcD neurons but not in the axon (Figure 4J-4L; Video S10), suggesting that the AIS of AcD neurons
168 still selectively blocks the transport of dendritic cargo.

169 To better understand the axonal cargo permissiveness and dendritic cargo filtering capacity of the AIS
170 in AcD neurons, we thoroughly analysed the trajectories of EGFP-Rab3A and TfR vesicles using a
171 Python-based program KYMOA (Figure S2; see STAR Methods for details). Quantitative analysis
172 showed that majority of the EGFP-Rab3A vesicles were mobile within the AIS of both AcD and nonAcD
173 neurons (nonAcD: 90% mobile, 10% stationary; AcD: 89% mobile, 11% stationary; Figure 4D), and no
174 significant difference was found on the average number or percentage of mobile vesicles between the

175 two cell types (Figure 4D; Figure S3A; Video S8 and S9). These mobile EGFP-Rab3A vesicles mainly
176 travelled anterogradely across the AIS towards the distal axon (nonAcD: 80% anterograde, 20%
177 retrograde; AcD: 70% anterograde, 30% retrograde; Figure 4G) and spent nearly 70% of the total
178 travelling time in processive runs (Figure S3B). Only a small portion of EGFP-Rab3A vesicles (nonAcD
179 neuron: 3%; AcD neuron: 5%; Figure S3C) underwent on average one direction change while traveling
180 anterogradely through the AIS (Figure S3C). During the rest of the total moving time, the anterogradely
181 transported EGFP-Rab3A vesicles in the AIS of both AcD and nonAcD neurons were either passively
182 diffusing back and forth (Figure S3B) or shortly pausing (Figure S3B) with on average three pauses per
183 minute, 3 s mean duration of each pause and 10 s of total pausing time (Figure 4I; Figure S3D). We
184 found that the anterogradely transported EGFP-Rab3A vesicles in the AIS of AcD neurons show slightly
185 longer mean run length, similar mean run duration and, therefore, higher mean run speed than in the
186 AIS of nonAcD neurons (Figure 4E, 4H and 4F). This finding suggests that, in AcD neurons, the axonal
187 cargoes are transported slightly faster across the AIS towards the distal axon. We did not observe any
188 difference on retrogradely transported EGFP-Rab3A vesicles in the AIS of AcD and nonAcD neurons
189 (Figure 4E, 4H and 4F), and EGFP-Rab3A vesicles in regular dendrites showed very limited mobility and
190 reduced trafficking (Figure 4E-4I; Figure S3C and S3D). In comparison to axonal cargoes, the dendritic
191 cargo TfR vesicles in both AcD and nonAcD neurons were immobile in the AIS but highly mobile in the
192 dendritic region (Figure 4M; Figure S3E and S3F; Video S10 and S11). Although a few moving TfR
193 vesicles were present at the AIS (Figure 4M; Figure S3E), these vesicles preferentially moved towards
194 the retrograde direction (Figure 4N) and showed higher percentage of pausing, longer pausing
195 duration, and slower velocity than in the dendritic regions (Figure 4O and 4P; Figure S3F-S3K),
196 indicating that their trafficking is severely impaired at the AIS. Almost no entries into the axon from
197 the AIS were observed (Figure 4K, 4L). These results suggest that the AIS of AcD neurons fully preserves
198 its selectivity towards dendritic cargoes, and the anterograde transport of axonal cargoes is equally
199 effective and processive as in the AIS of nonAcD neurons.

200 Interestingly, we noticed that both axonal cargo EGFP-Rab3A and dendritic cargo TfRs were actively
201 transported at the stem dendrite of AcD neurons (Figure 4; Video S8 and S10). The trafficking velocity
202 of EGFP-Rab3A and TfR vesicles highly resembled that in the AIS and dendrites (Figure 4F; Figure S3K),
203 respectively, except that the average run length and run duration of both cargoes were much shorter
204 at the stem dendrite (Figure 4E and 4H; Figure S3I-S3K). Since the stem dendrite is in general shorter
205 than the AIS and the dendrites, this reduction of run length and duration is very likely caused by the
206 difference in physical length.

207 **The AIS of AcD neurons does not undergo activity dependent plasticity and receives less**
208 **inhibitory innervation**

209 The AIS has been shown to regulate neuronal homeostasis via two types of plasticity: rapid and chronic
210 plasticity.[22,23] The rapid plasticity occurs when increasing neuronal activity for a few hours and induces
211 AIS length shortening.[22] The chronic plasticity requires high neuronal activity for at least two days and
212 causes the AIS to shift towards the distal axon but without any change in length.[23] Previous studies
213 showed that the dendritic origin of the axon resulted a different excitability patterns of AcD
214 neurons.[26,28] This motivated us to investigate whether the AIS of AcD neurons would regulate cellular
215 homeostasis in a different manner. The elevated extracellular K^+ concentration is an effective way to
216 globally depolarise membrane potential of neurons.[36] We added KCl into conditioned medium to
217 increase extracellular K^+ up to 15 mM and stimulated DIV12 neurons for 3 and 48 hours to induce rapid
218 and chronic AIS plasticity[22,23], respectively (Figure S4A). To rule out possible effects caused by the
219 change in osmolarity, we replaced KCl with NaCl in control groups (Figure S4A). For comparison, we
220 silenced the baseline synaptic activity by blocking voltage gated sodium channels (VGSCs) with 1 µM
221 tetrodotoxin (TTX) (Figure S4A). As read out of AIS plasticity, we stained AIS with AnkG and measured
222 its fluorescent intensity to define the AIS length and AIS distance (Figure S4B and S4C). Using a
223 previously published method[22,23], we considered the start and end of the AIS as the location where

224 AnkG fluorescence intensity drops below 40% of the maximum intensity (Figure S4C). The AIS distance
225 is measured as the distance from the start of the axon to the beginning of the AIS (Figure S4C).

226 In nonAcD neurons, we indeed observed a distal shift of the AIS after 48 hours of KCl treatment (Figure
227 5A and 5B), meaning that the increased extracellular K^+ concentration successfully triggered an AIS
228 plasticity effect. However, we did not observe the previously reported AIS length reduction after 3
229 hours of KCl treatment (Figure 5A and 5B; Figure S4D). Strikingly, in AcD neurons, neither the 48 hours
230 KCl treatment shifted the AIS towards the distal axon tip, nor was the AIS length reduced after 3 hours
231 KCl treatment (Figure 5C and 5D), suggesting that the AIS in AcD neurons is insensitive to high activity
232 levels. Like previously reported[22,23], both NaCl and TTX showed no effect on AIS length after 3 hours
233 (Figure 5), and on AIS position after 48 hours in both AcD and nonAcD neurons (Figure 5). However,
234 we noticed that after 48 hours incubation, the TTX specifically increased AIS length in nonAcD neurons
235 (Figure S4E) leaving the length of AIS in AcD neurons unchanged (Figure S4F). This finding indicates
236 that the AIS also undergo structural remodelling when nonAcD neurons encounter extremely low
237 activity levels. On the other hand, it further supports the statement that the AIS of AcD neurons is
238 insensitive to activity changes.

239 The interneurons form axo-axonal inhibitory synapses with the AIS of excitatory neurons to modulate
240 their excitability.[24] We next asked if the density of inhibitory synapses is different at the AIS of AcD
241 neurons. Hypothetically, lower amount of axo-axonal inhibitory synapses at the AIS could possibly
242 assist AcD neurons to generate APs more easily during global peri-somatic inhibition in addition to
243 their uncanonical route for AP initiation. To quantify the number of inhibitory synapses, we labelled
244 the pre- and post- synaptic compartments by staining voltage gated GABA transporters (VGAT) and
245 gephyrin, respectively. In comparison to nonAcD neurons, we found fewer numbers of both VGAT and
246 gephyrin at the AIS of AcD neurons (Figure 6A and 6C). We also quantified the amount of excitatory
247 pre- and post- synapses at the AIS of AcD neurons to test if there are any differences in the excitatory
248 synapses. However, quantification of excitatory pre- and post- synaptic marker homer-1 and voltage
249 gated glutamate transporter (VGLUT) showed that the number of excitatory synapses at the AIS of AcD

250 neurons is equally low as in nonAcD neurons (Figure 6B and 6D). Together, these results indicate that

251 AcD neurons indeed receive fewer inhibitory inputs than nonAcD neurons at the AIS.

Discussion

AcD neurons have been widely observed across species ranging from invertebrates to vertebrates.[25–28,37] Only recently, the abundance of AcD neurons in certain brain areas was characterised and their role in memory consolidation was discovered.[26–28] Despite their importance in brain functions, AcD neurons remain largely unexplored from the cell biology perspective. Considering the heterogeneity of development between cell types, it is an intriguing question whether the morphogenesis of AcD neurons is an intrinsic process or it is dependent on guidance cues. Furthermore, it is unclear how the AcD and axon are differentiated, and to what extend the AIS branching from a dendrite is similar to the AIS emerging from the soma.

In this study, we describe the developmental sequence leading to the formation of dendrite-derived axons, and explore the cytoskeletal organisation of AcD neurons. We investigate the timing of AIS assembly and its role in neuronal polarity, synaptic innervation and plasticity in AcD neurons. We show that the development of AcD neuron is an intrinsically encoded process, where a single precursor neurite gives rise to both the axon and the AcD. Although multiple strategies exist for axon and AcD differentiation, our data clearly indicate that AcD neurons still follow the general developmental sequence to first establish the axon and then the dendrites.[2] The molecular mechanisms involved in AcD neuron development remain unknown. Several intrinsic polarity effectors, such as Shootin1[38], Ras proteins[39] and Rho GTPases[40], have been found to guide the formation of axon and dendrites in nonAcD neurons. The cytoskeleton dynamics have also been shown to help neuron determine the identity of a nascent neurite.[38,41,42] Thus, future efforts should focus not only on investigating specific proteins and associated signalling pathways that instruct AcD neuron morphogenesis, but also on the cytoskeleton dynamics in the precursor neurite where the axon and AcD are derived from. It is also possible that the ability to grow an axon from a dendrite comes from AcD neurons being a different subtype of pyramidal neurons. It would be of interest to perform single cell RNA sequencing to analyse gene expression profile of AcD neurons and possibly identify specific markers of this cell type.

277 The uniform MT plus end orientation and high ratio of acetylation/tyrosination of axonal MTs are
278 instructive for specific kinesin motors, such as kinesin-1, to correctly deliver vesicles containing axonal
279 cargoes.[5,43] We show that AcD neurons preserve an axon-like MT arrangement at the stem dendrite.
280 Since the stem dendrite is the only channel connecting soma and axon, this axon-like MT organisation
281 is of importance to ensure that axonal cargoes can travel through the stem dendrite region to be
282 targeted to the axon. Indeed, our live-imaging data demonstrate that in AcD neurons, the axonal Rab3
283 vesicles are smoothly transported through the stem dendrite before they enter the axon, whereas they
284 are highly immobile in other dendrites.

285 To prevent the entry of dendritic cargoes into the axon, neurons build the AIS at the interface between
286 axon and soma to selectively block MT-based transport of vesicles containing dendritic proteins.[13,21]
287 This selectivity of the AIS towards dendritic cargoes has been shown to rely on F-actin structures and
288 the actin-based motor protein Myosin V.[11,12] We demonstrate that, in AcD neurons, the F-actin
289 nanostructure at the AIS is similarly arranged as in nonAcD neurons. Consistently, axonal and dendritic
290 cargo trafficking assay in AcD neurons show that vesicles containing dendritic cargoes are trapped at
291 the AIS to the same extend as at the AIS emanating from the soma. These results suggest that the
292 dendritic axon origin has no impact on AIS function being a cytoplasmic protein filter that prevents
293 entry of dendritic cargoes into the axon.

294 Single-cell patch clamp in nonAcD hippocampal excitatory neurons have demonstrated that the rapid
295 and chronic structural plasticity of the AIS fine tunes neuronal excitability to prevent neurons from
296 going epileptic.[22,23] Our results show that the AIS in hippocampal AcD excitatory neurons does not
297 undergo any structural plasticity upon changes of neuronal activity, suggesting that hippocampal AcD
298 neurons may employ a different strategy to maintain cellular homeostasis than nonAcD neurons or be
299 less adoptive which makes them more susceptible to pathological conditions. Of note, we also did not
300 observe any rapid AIS plasticity effect in nonAcD neurons. This might be due to cell type specificity, as
301 a previous study showed that rapid AIS plasticity occurs mainly in hippocampal dentate granule cells
302 (DGCs) but not in principal neurons.[22] Another possibility is that certain post-synaptic signalling factors

303 are required to trigger rapid AIS plasticity, as KCl stimulation mainly changes the membrane potential
304 to depolarise neurons but is lacking any input specificity.[36]

305 The underlying mechanisms of the activity-dependent AIS plasticity is still ambiguous. Up to date,
306 several lines of evidence suggest the significance of Ca^{2+} signalling in this process. The activity of a Ca^{2+}-
307 and calmodulin-dependent protein phosphatase calcineurin has been shown to be relevant for AIS
308 plasticity, and specifically blocking voltage gated Ca^{2+} channels (VGCCs) disrupts the distal shift of AIS
309 in hippocampal excitatory neurons.[23] Along with these lines, we found that the number of COs is
310 decreased in the AIS of AcD neurons. Since COs putatively regulate Ca^{2+}-storage and release at the AIS
311 of several neuronal subtypes[18,19,33], this reduction of the CO number might influence Ca^{2+} handling in
312 AcD neurons, which then modulate the AIS plasticity. Supportively, a recent study showed that the
313 number of COs is decreased when induce rapid AIS plasticity in rat hippocampal DGCs.[44] In the future,
314 one should more thoroughly investigate the mechanistic role of COs in the process of AIS plasticity.
315 Interestingly, several new AIS specific proteins were recently detected via proximity labelling assay.[45]
316 It would be interesting to investigate whether they are involved in controlling AIS plasticity and
317 compare between the two types of neurons. Another direction to be explored is the link between
318 extracellular matrix proteins (ECMs) and AIS structural plasticity in AcD neurons, as the plasma
319 membrane of the AIS is also enriched with cell adhesion molecules (CAMs). These CAMs could possibly
320 work in concert with ECMs and therefore limit the shift of AIS in AcD neurons.
321 The inhibitory synapses at the AIS of excitatory neurons is an important modulator for the activation
322 and silencing of specific neuronal circuits.[24] Our data showed that the AIS of AcD neuron has less
323 inhibitory innervation than in nonAcD neurons. This result supports the fact that AcD neurons can
324 evade peri-somatic inhibition during network oscillation. It would be interesting to see in the future
325 which type of interneurons are innervating the AIS of AcD neurons and how this contributes to the
326 higher intrinsic excitability of AcD neurons.
327

Acknowledgements

We would like to thank Bianca Slivinschi for experimental assistance and help with data analysis, Zhengyue Zhang (MUNI-CEITEC, Brno) for help with python scripting, Tomas Fanutza (ZMNH, Hamburg) and Karin Ruban (CSSB, Hamburg) for help with sample preparation and transport between the institutions, Dr. Antonio Virgilio Failla (UMIF, Hamburg) for access and help with use of STED confocal microscope, and Dr. Christian Conze (LIV, Hamburg) for help with microscope access at the LIV. We acknowledge Dr. Anja Konietzny (ZMNH, Hamburg) for technical assistance and valuable feedback on the manuscript, Dr. Ingke Braren (UKE Virus Facility) for rAAV production. This research is supported by the Landesforschungsförderung Hamburg (LFF to MM and KG) and by the German research foundation (Excellence Strategy – EXC-2049–390688087 to MM, DFG FOR5228 to MM and DFG FOR2419 to MM and KG).

Author contributions

Designed experiments (YH, RT, KG, MM), performed experiments (YH), analyzed and interpreted data (YH, KG, MM), developed the manuscript concept (YH, KG, MM), wrote the first draft (YH, MM), reviewed and edited the paper (YH, RT, KG, MM) and acquired funding (KG, MM)

Competing interests

The authors declare no competing financial interests.

Materials & Correspondence

Materials (constructs) can be requested from Marina Mikhaylova; correspondence can be addressed to Kay Grünewald and Marina Mikhaylova.

Figure legends

Figure 1. Development of neurons with axon carrying dendrite.

(A) Representative images of hippocampal primary neurons in dissociated cultures demonstrating the timeline of AIS formation in nonAcD and AcD neurons. White arrowhead indicates AIS labelled by AnkG staining; yellow and pink arrowhead indicates AcD and stem dendrite of AcD neuron respectively (labelled by MAP2); cyan arrowhead indicates regular dendrite. Scale bar is 20 μm.

(B) Schematic of AcD neuron. Black dashed line indicates the edge of soma; orange dashed line indicates the beginning of an axon.

(C) Percentage of nonAcD and AcD neurons in dissociated culture at age of DIV 5 and DIV7. n = 6 coverslips from 3 independent cultures, DIV5: 83 AcD neurons out of 427 cells, DIV7: 47 AcD neurons out of 387 cells.

(D) Time-lapse images of developing nonAcD and AcD neurons. Precursor neurite in AcD neuron grow as axon and collateral from the precursor neurite develop as AcD. Orange arrowhead indicates precursor neurite of AcD neuron; blue arrowhead indicates precursor neurite of nonAcD neuron; white arrowhead indicates axon; yellow and pink arrowhead indicates AcD and stem dendrite of AcD neuron, respectively. Scale bar is 20 μm. Cell body with dendrites and the AIS are labelled by MAP2 and AnkG staining, respectively. Related to Video S1 and S2.

(E and F) Percentage of AcD neurons which develop AcD and axon via collateralization and bifurcation of precursor neurite (E) and time points of collaterals formed at precursor neurite of AcD neuron (F). 1 independent culture, nonAcD: n= 25 cells, AcD: n= 27 cells.

(G) Percentage of precursor neurite in AcD neurons grew as axon or as AcD. 1 independent culture, AcD: n= 23 cells.

(H) Percentage of nonAcD and AcD neuron form collaterals at the proximal region of precursor neurite during development. 1 independent culture, nonAcD: n= 25 cells, AcD: n= 23 cells.

(I) Schematic of AcD neuron development.

377 **Figure 2.** MT orientations and distribution on dynamic and stable MTs in AcD neurons.

378 (A) Left panel: Maximum intensity projection of DIV14 nonAcD and AcD neuron transfected
379 with EB3-Tdtomato for visualisation of MT plus ends. The AIS is live labelled with anti-NF-
380 CF640R antibody. White arrowhead indicates the AIS and white arrow indicates the axon.
381 Cyan arrowhead indicates regular dendrite (Regular D); yellow and pink arrowhead indicates
382 AcD and stem dendrite of AcD neuron, respectively. Scale bar is 10 µm. Right panel: 5 minutes
383 time projection and kymograph of EB3-Tdtomato in the AIS, axon and regular dendrite
384 (Regular D) of nonAcD and AcD neuron shown in the left panel. Scale bar is 10 µm. Kymograph
385 scale is 10 s (vertical) and 2 µm (horizontal).

386 (B) 5 minutes time projection and kymograph of EB3-Tdtomato in AcD and stem dendrite (Stem
387 D) of AcD neuron shown in (A). Scale bar is 5 µm. Kymograph scale is 10 s (vertical) and 2
388 µm (horizontal).

389 (C) Percentage of MT plus end orientations in different regions of nonAcD and AcD neurons.
390 Mean ± SEM, 3 independent experiments, AIS (nonAcD) n = 23, AIS (AcD) n = 17, axon
391 (nonAcD) n = 21, axon (AcD) n= 15, stem dendrite (Stem D) n = 19, AcD n = 17, regular
392 dendrite (Regular D) n = 67.

393 (D) Top row: Representative confocal images of DIV10 nonAcD and AcD neurons stained for
394 tyrosinated and acetylated tubulin and the AIS marker TRIM46. Scale bar is 10 µm. Bottom
395 row: Single plane 2D gSTED image of tyrosinated and acetylated MTs corresponding to ROIs
396 in top row. Scale bar is 2.5 µm.

397 (E) Intensity profile of tyrosinated and acetylated MTs indicated by white dashed lines in (D)
398 bottom row.

399 **Figure 3.** F-actin organisation at the AIS of nonAcD and AcD neurons.

400 (A) Top row: Representative confocal images of DIV14 nonAcD and AcD neuron stained with
401 the AIS marker βIV-spectrin and F-actin probe Phalloidin-Atto647N. Scale bar is 10 µm. Bottom
402 row: Single plane 2D gSTED image of F-actin in the AIS of nonAcD and AcD neurons
403 (corresponding zoom-ins of yellow dashed square in top row). Scale bar is 1 µm. Red
404 arrowhead indicates F-actin patch. Black dashed line indicates F-actin rings.

405 (B) Left panel: Intensity profile of F-actin rings along the longitudinal axis of the AIS in nonAcD
406 and AcD neuron, corresponding to black dashed lines in (A) bottom row. Right panel:
407 Quantification of distance between F-actin rings at the AIS of nonAcD and AcD neuron. Mean
408 ± SEM, 3 independent experiments, nonAcD: n= 45 profiles from 12 cells, AcD: n= 67 profiles
409 from 18 cells.

410 (C) Representative images of cisternal organelle (CO) labelled by synaptopodin (Synpo)
411 staining at the AIS of DIV21 nonAcD and AcD neurons. Scale bar is 10 µm. Inset: Zoom-ins
412 corresponding to white dashed rectangular. Black dashed lines indicate the edge of AIS. Scale
413 bar is 5 µm.

414 (D) Quantification of Synpo puncta at the AIS of nonAcD and AcD neurons. Mean ± SEM, 3
415 independent experiments, nonAcD: n= 92 cells, AcD: n= 57 cells.

416 Mann-Whitney test: not significant (n.s.) $p > 0.05$, $^{**}p < 0.01$.

417 **Figure 4.** Role of the AIS in polarized cargo trafficking in AcD and nonAcD neurons

418 (A) Representative images of nonAcD and AcD neurons expressing a pre-synaptic vesicle
419 marker EGFP-Rab3A and labelled with anti-NF-CF640R (NF). White dashed line indicates the
420 recorded area after photobleaching; white arrowhead indicates the AIS; pink, yellow and cyan
421 arrowheads indicate the stem dendrite, AcD and regular dendrite of AcD neuron, respectively.
422 Scale bar is 15 μm.

423 (B) Representative kymographs showing trajectories of EGFP-Rab3A vesicles travelling in the
424 AIS of nonAcD neuron shown in (A), corresponding to area indicated by white dashed line.
425 Scale is 10 s (vertical) and 2 μm (horizontal). Anterograde direction is from cell body to the
426 distal tip of corresponding neuritic process, retrograde direction is the opposite.

427 (C) Representative kymographs showing trajectories of EGFP-Rab3A vesicles travelling in the
428 stem dendrite (Stem D), AIS and regular dendrite (Regular D) of AcD neuron shown in (A),
429 corresponding to area indicated by white dashed line. Scale is 10 s (vertical) and 2 μm
430 (horizontal). Anterograde and retrograde direction is the same as in (B).

431 (D and G) Motility and directionalities of EGFP-Rab3A vesicles in the AIS of nonAcD neuron,
432 the AIS and stem dendrite (Stem D) of AcD neuron, and the regular dendrite (Regular D) of
433 both nonAcD and AcD neurons. (D) Percentage of running and stationary EGFP-Rab3A
434 vesicles. (G) Percentage of EGFP-Rab3A vesicles running towards anterograde and
435 retrograde direction. Mean ± SEM, 7 independent experiments, AIS (nonAcD): n = 42 cells,
436 AIS (AcD) n = 42 cells, Stem D: n= 28 cells, Regular D: n= 27 cells.

437 (E, F and H) Average length (E), duration (H) and velocity (F) of EGFP-Rab3A vesicles running
438 towards anterograde and retrograde direction within the AIS of nonAcD neuron, the AIS and
439 stem dendrite (Stem D) of AcD neuron, and the regular dendrite (Regular D) of both nonAcD
440 and AcD neurons. Mean ± SEM, 7 independent experiments, Anterograde: AIS (nonAcD) n =
441 42 cells, AIS (AcD) n = 41 cells, Stem D n= 28 cells, Regular D n= 26 cells, Retrograde: AIS
442 (nonAcD) n = 25 cells, AIS (AcD) n = 37 cells, Stem D n= 17 cells, Regular D n= 20 cells.

443 (I) Average number of pauses and total pausing duration of EGFP-Rab3A vesicles travelling
444 in the indicated regions of nonAcD and AcD neuron regardless of directions. Mean ± SEM, 7
445 independent experiments, AIS (nonAcD) n = 42 cells, AIS (AcD) n = 42 cells, Stem D n= 28
446 cells, Regular D n= 27 cells.

447 (J) Representative images of nonAcD and AcD neurons labelled with anti-NF-CF640R (NF)
448 for AIS and TfR ligand Transferrin-Alexa568. White dashed line indicates recorded area; white
449 arrowhead indicates the AIS; cyan arrowhead indicates regular dendrite of nonAcD neuron;
450 yellow and pink arrowhead indicates the AcD and stem dendrite of AcD neuron, respectively.
451 Scale bar is 15 μm.

452 (K) Representative kymographs showing trajectories of TfR vesicles travelling in the AIS, axon
453 and regular dendrite (Regular D) of nonAcD neuron shown in (A), corresponding to the area
454 indicated by white dashed line. Scale is 5 s (vertical) and 2 μm (horizontal). Anterograde
455 direction is the same as in (B).

456 (L) Representative kymographs showing trajectories of TfR vesicles travelling in the AIS, axon,
457 stem dendrite (Stem D) and AcD of AcD neuron shown in (A), corresponding to the area

indicated by white dashed line. Scale is 5 s (vertical) and 2 μm (horizontal). Anterograde and retrograde direction is the same as in (B).

(M and N) Motility and directionalities of TfR vesicles in the AIS of nonAcD neuron, the AIS, stem dendrite (Stem D) and AcD of AcD neuron, and the regular dendrite (Regular D) of both nonAcD and AcD neurons. (M) Percentage of running and stationary TfR vesicles. (N) Percentage of TfR vesicles running towards anterograde and retrograde direction. Mean ± SEM, 5 independent experiments, AIS (nonAcD) n = 25 cells, AIS (AcD) n = 23 cells, Stem D n= 23 cells, AcD n = 19 cells, Regular D n= 56 cells.

(O and P) Average number of pause (O) and total pausing duration (P) of TfR vesicles travelling in the indicated regions of nonAcD and AcD neuron regardless of directions. Mean ± SEM, 5 independent experiments, AIS (nonAcD) n = 25 cells, AIS (AcD) n = 23 cells, Stem D n= 23 cells, AcD n = 19 cells, Regular D n= 56 cells.

One-way ANOVA with Tukey's multiple comparisons test, no significance (n.s.) $p > 0.05$, **$p < 0.01$, ***$p < 0.001$, ****$p < 0.0001$.

472 **Figure 5.** Rapid and chronic plasticity of the AIS in AcD neurons.

473 (A) Representative images of the AIS in nonAcD neurons upon induction of rapid (upper row)
474 and chronic (bottom row) plasticity. Neurons were treated with KCl for depolarization, NaCl as
475 control and TTX for silencing. Red arrowheads in upper row indicate the start and end of AIS.
476 Red dashed line in bottom row indicates the start of the axon. Scale bar is 10 µm.

477 (B) Measurement of AIS length and AIS distance in nonAcD neurons treated with KCl
478 (depolarization), NaCl (control) and TTX (silencing) for 3 and 48 hours. Mean ± SEM, 3
479 independent experiments, Rapid plastiicity: n (KCl) = 298 cells, n (NaCl) = 264 cells, n (TTX)
480 = 306 cells, Chronic plasticity: n (KCl) = 189 cells, n (NaCl) = 192 cells, n (TTX) = 202 cells,

481 (C) Representative images of the AIS in AcD neurons upon induction of rapid (upper row) and
482 chronic (bottom row) plasticity. Neurons were treated with KCl for depolarization, NaCl as
483 control and TTX for silencing. Red arrowheads in upper row indicate the start and end of AIS.
484 Red dashed line in bottom row indicates the start of the axon. Scale bar is 10 µm.

485 (D) Measurement of AIS length and AIS distance in AcD neurons treated with KCl
486 (depolarization), NaCl (control) and TTX (silencing) for 3 and 48 hours. Mean ± SEM, 4
487 independent experiments, Rapid plasticity: n (KCl) = 48 cells, n (NaCl) = 40 cells, n (TTX) =
488 41 cells, Chronic plasticity: n (KCl) = 73 cells, n (NaCl) = 75 cells, n (TTX) = 66 cells.

489 One-way ANOVA with Tukey's multiple comparisons test, no significance (n.s.) $p > 0.05$, ****p
490 < 0.0001.

491 **Figure 6.** Inhibitory and excitatory synaptic innervation of the AIS in nonAcD and AcD neurons.

492 (A) Representative images of nonAcD and AcD neurons stained with markers for pre- and
493 post-synaptic compartments of an inhibitory synapse (VGAT and gephyrin, respectively), for
494 AIS (TRIM46), and for somato-dendritic compartment (MAP2). Upper row: Gephyrin. Lower
495 row: VGAT. Scale bar is 10 µm. Inset: corresponding zoom-ins of white dashed rectangular.
496 Scale bar is 5 µm. Black arrowheads indicate corresponding marker for pre- and post-inhibitory
497 synapse.

498 (B) Representative images nonAcD and AcD neurons stained with markers for pre- and post-
499 synaptic compartments of an excitatory synapse (VGLUT and homer-1, respectively), for AIS
500 (TRIM46 or AnkG), and for somato-dendritic compartment (MAP2). Upper row: Homer-1.
501 Lower row: VGLUT. Scale bar is 10 µm. Inset: corresponding zoom-ins of white dashed
502 rectangular. Scale bar is 5 µm. Black arrowheads indicate corresponding marker for pre- and
503 post-excitatory synapse.

504 (C) Number of gephyrin and VGAT puncta per 5 µm at the AIS of nonAcD and AcD neurons.
505 Mean ± SEM, 4 independent experiments, gephyrin: n (nonAcD) = 71 cells, n (AcD) = 56 cells,
506 VGAT: n (nonAcD) = 70 cells, n (AcD) = 75 cells.

507 (D) Number of Homer-1 and VGLUT puncta per 5 µm at the AIS of nonAcD and AcD neurons.
508 Mean ± SEM, 3 independent experiments for Homer-1, 4 independent experiments for VGLUT,
509 Homer-1: n (nonAcD) = 74 cells, n (AcD) = 78 cells, VGLUT: n (nonAcD) = 67 cells, n (AcD) =
510 50 cells.

511 Mann-Whitney test: not significant (n.s.) $p > 0.05$, *$p < 0.05$, ***$p < 0.0001$.

512 **Methods**

513 **Animals**

514 Wistar Unilever HsdCpb:WU (Envigo) rats were used in this study. Rats were bread and kept at the
515 animal facility of the University Medical Center Hamburg-Eppendorf, UKE, Hamburg, Germany. Animal
516 experiments were carried out in accordance with the European Communities Council Directive
517 (2010/63/EU) and the Animal Welfare Law of the Federal Republic of Germany (Tierschutzgesetz der
518 Bundesrepublik Deutschland, TierSchG) approved by the city-state Hamburg (Behörde für Gesundheit
519 und Verbraucherschutz, Fachbereich Veterinärwesen, from 21.04.2015, ORG781 and 1035) and the
520 animal care committee of the University Medical Center Hamburg-Eppendorf.

521 **Primary hippocampal neuron preparation and transfections**

522 Primary rat hippocampal neurons were prepared and maintained as described previously[20]. Briefly,
523 hippocampi were extracted from E18 rat embryos and treated with 0.25% trypsin for 15 min at 37°C.
524 Afterwards, hippocampi were physically dissociated by pipetting through a 26G needle and filtered to
525 remove large clumps. The cell suspensions were then plated on poly-l-lysine -coated 18 mm glass
526 coverslips or 35 mm glass bottom petri dish at a density of 20,000 cells (extra low density) or 40,000
527 cells (low density) or 60,000 cells (high density) per 1 ml in DMEM supplemented with 10% fetal calf
528 serum and antibiotics. After 1 hour, the plating medium was replaced by BrainPhys neuronal medium
529 supplemented with SM1 and 0.5 mM glutamine. Cells were grown at 37°C with 5% CO2, and 95%
530 humidity.

531 For microtubule orientation experiment, primary neurons were transfected with EB3-Tdtomato at
532 days in vitro (DIV) 14 by using lipofectamine 2000. Conditioned neuronal medium was removed and
533 stored at 37°C with 5% CO2 before transfection. Neurons were then incubated with transfection
534 medium (transfection mixture in BrainPhys medium without supplements) at 37°C with 5% CO2 for 1

535 hour. After incubation, the transfection medium was exchanged back to conditioned medium, and
536 neurons were imaged 12 hours after. For EGFP-Rab3 trafficking experiment, primary neurons were
537 infected with rAAV9-syn-EGFP-Rab3 virus (final concentration: 1.38E+10 vg/ml) at DIV5 and imaged at
538 DIV7.

539 **Constructs and recombinant adeno-associated viruses**

540 Detailed information of constructs and virus used in this study can be found in the key resource table.
541 The EB3-Tdtomato construct was obtained from Addgene (Addgene plasmid #50708;
542 http://n2t.net/addgene:50708; RRID:Addgene_50708). For rAAV9-syn-EGFP-Rab3A construct, full
543 length Rab3A sequence was amplified from EGFP-Rab3A vector (Addgene plasmid # 49542) using PCR.
544 The amplified sequence was then cloned onto a recombinant adeno-associated virus (rAAV) backbone
545 with an EGFP tag behind a human synapsin promotor using Cold Fusion cloning kit. The Rab3A
546 sequence is placed behind EGFP sequence for N-terminal tagging of Rab3A. After verification by
547 sequencing, rAAV9 were produced by the UKE virus facility.

548 **Immunocytochemistry (ICC)**

549 Neurons were fixed in 4% Roti-Histofix (Carl Roth), 4% sucrose in PBS for 10 min at 37°C. The fixation
550 reagent was removed, and coverslips were washed three times with PBS. Subsequently, neurons were
551 permeabilized in 0.2% Triton X-100 in PBS for 10 min, then washed three times in PBS and blocked for
552 45 min at RT with blocking buffer (BB: 10% horse serum, 0.1% Triton X-100 in PBS). Incubation with
553 primary antibodies was performed in BB at 4°C overnight. After 3× wash in PBS, neurons were
554 incubated with corresponding secondary antibodies in BB for 1.5 h at RT and unbound antibodies were
555 washed out using PBS. In order to distinguish dendrites from axons, pre-conjugated MAP2-Alexa488
556 antibody diluted in BB was then applied to neurons for 1.5 h at RT. Finally, coverslips were washed
557 three times in PBS (10 min interval), one time in H_2O for 10 s and mounted on microscope slides with
558 Mowiol.

559 **Spinning disc confocal microscopy**

560 For live imaging of EB3-Tdtomato, EGFP-Rab3A and Transferrin receptors (TfRs), spinning-disc confocal
561 microscopy was performed on a Nikon Ti-2E controlled by NIS Elements 5.2 software. Illumination was
562 done by 488 nm, 561 nm, and 642 nm excitation lasers from Omicron laser unit coupled to a Yokogawa
563 CSU-W1 spinning disc unit. Emission was collected through a bandpass filter (Semrock,
564 442/525/609/700 nm) on an Andor iXon ultra 888 EMCCD camera. Use of 100x TIRF objective (Nikon,
565 ApoTIRF 100x/1.49 oil) achieved a pixel size of 130 nm.

566 For imaging of neuronal development, phase contrast imaging was performed on a Nikon Ti-2E
567 microscope controlled by NIS Elements 5.2 software. The microscope was equipped with an
568 Omicron laser unit coupled to a Yokogawa Borealis-enhanced CSU-W1 spinning disc unit,
569 transmitted illumination and an Andor iXon ultra 888 EMCCD camera. Samples were
570 illuminated by transmitted light and imaged via 40X objective (Nikon, ApoLWD Lambda
571 40x/1.15 WI). The final fluorescent map was acquired through the same objective with laser
572 illumination at wavelength of 488 nm and 642 nm. Both microscopes were equipped with a
573 live imaging system from OKO lab and live imaging was performed at 37°C with 5% CO2 and
574 95% humidity.

575 **Laser scanning confocal microscopy and STED imaging**

576 Fixed and stained primary hippocampal neurons were imaged at a Leica SP8 confocal microscope (Leica
577 microsystems, Mannheim, Germany). The microscope was controlled by Leica Application Suite X
578 (LASX) software and equipped with a white light laser. Samples were imaged using a 63x oil objective
579 (Leica, 63x HCX PL APO /1.40 oil). Fluorophores were excited at desired wavelength and signals were
580 detected using HyD detectors. Tile scans of maximum 2 mm x 2 mm areas were performed to increase
581 the chance of finding AcD neurons. A single z-stack tile was acquired with dimension of 1024 x 1024

582 pixels, pixel size of 80 nm, pixel depth of 16 bit, and z-step size of 0.5 µm. Tiles were merged by LASX
583 function Mosac Merge with 10% overlap.

584 An Abberior gatedSTED system equipped with a 405 to 640 nm pulsed laser and a 60x oil objective
585 (Nikon, P-APO 60x/1.40 oil) was used for confocal and gated STED imaging. For excitation, 640 nm laser
586 was used for Atto647N/Abberior Star 635p, 561 nm laser was used for Abberior Star 580, and 488 nm
587 laser was used for Alexa 488. STED was achieved with a 775 nm pulsed depletion laser for
588 Abberior Star 580, Abberior Star 635p and Atto647N. Emission spectra were collected
589 between 650-720 nm, 605-625 nm and 500-550 nm. Detector time gates were set to 8 ns for
590 all fluorophores. Images were acquired as single planes with a pixel size of 20 x 20 nm (x and
591 y) and 16-bit pixel depth. The corresponding confocal images were acquired with identical
592 settings.

593 **Classification of AcD and nonACD neurons**

594 AcD and nonAcD neurons were classified based on MAP2 and AnkG stainings which label somato-
595 dendritic compartment and the AIS of axon, respectively. The distance from the starting point of an
596 axon to the adjacent edge of corresponding cell body was referred as axon distance in this study and
597 used as main factor for AcD neuron classification (Figure 1B; Figure S1D). To measure the axon
598 distance, axon and cell body of a neuron was defined individually based on AnkG and MAP2 signal. A
599 2 pixel wide segmented line was then drew along the longitudinal axis of stem dendrite to connect the
600 beginning of the axon and the ending edge of the cell body (Figure 1B). The length of the segmented
601 line represents axon distance. If the axon origin was not parallel to the ending edge of soma (Figure
602 S1D), the axon distance was then considered as the distance from the edge of soma to the axis
603 perpendicularly extended from the centre of the axon origin (Figure S1D). Neurons with axon distance
604 larger than 3 µm was consider as AcD neuron. The AcD and nonAcD neuron was classified in the same
605 manner through the entire study, unless otherwise stated.

606 **Assessment of AcD neuron population in dissociated cultures and the timeline of AIS**
607 **formation**

608 Dissociated neurons (60,000 cells/ml) were fixed at DIV3, DIV5, DIV7 and DIV12 and immunostained
609 with anti-MAP2-Alexa488 antibody to label the cell body and dendrites. Antibodies against AnkG was
610 used to visualise the AIS. Tile scan of large area was taken for both MAP2 and AnkG channels with 1%
611 laser power and 5 µm depth in z. Total number of neurons at age of DIV5 and DIV7 was counted from
612 all tile scan images. The number of AcD neuron was then counted from the same images and divided
613 by total number of neurons to calculate percentage of AcD neuron population.

614 **Time-lapse imaging to visualise neuronal development in culture**

615 High density neurons (60,000 cells/ml) were cultured on a 35 mm glass bottom petri dish with 20 x 20
616 mm grid coordinates. A 3 mm diameter hole was drilled on the lid of the petri dish for replenishment
617 of conditioned medium. To prevent medium evaporation during the entire imaging period,
618 conditioned medium was refilled on daily basis. Additional three 35 mm petri dishes were filled with
619 distilled H_2O and placed in the live imaging chamber without lids to increase atmospheric humidity.
620 The H_2O petri dishes was refilled every 12 hours to maintain proper humidity level in the live imaging
621 chamber.

622 Developmental sequences were recorded 6 hours post plating. Dishes were placed on a spinning disc
623 confocal microscope and imaged for 5 days every 3 hours. To increase the number of AcD neurons, a
624 7 x 7 mm area was scanned spirally starting from the centre of the grid coordinates. On day 5, neurons
625 were fixed and immunostained with pre-conjugated anti-MAP2-Alexa488 and anti-AnkG antibody to
626 label dendrites and the AIS, respectively. A single plan fluorescent image of both MAP2 and AnkG
627 channels was then taken at the same scanned area with 20% laser power and 200 ms exposure time.
628 The fluorescent image was used as a final map for selection of AcD and nonAcD neurons, and the
629 developmental sequence of selected neurons was retrieved according to grid coordinates. The

630 formation and growth of AcD and axon in AcD neurons was analysed manually by going through the
631 corresponding developmental sequence frame by frame. All analysis was performed on Fiji.

632 **F-actin staining and analysis of periodic membrane actin cytoskeleton of the AIS**

633 For F-actin staining, extra low density neurons (20,000 cells/ml) were plated on 18 mm high precision
634 glass coverslips, fixed on DIV14, and immunostained with anti-βIV-Spectrin and pre-conjugated anti-
635 MAP2-Alexa488 antibody to label the AIS and dendrites, respectively. Following the antibody staining,
636 the F-actin was labelled by incubation with phalloidin-Atto647N (1:100 dilution in PBS) at 4°C
637 overnight. Following 3x wash with PBS, coverslips were mounted using moviol and imaged on an
638 Abberior gatedSTED system as described above.

639 Peak Cal 3.0, a custom-written python-based script (see key resource table), was used to measure the
640 F-actin periodicity at the AIS. Briefly, AIS regions with less phalloidin-Atto647N background signal were
641 selected manually from the STED image. A 3 x 3 pixel segmented line profile was drew at the selected
642 regions along the longitudinal axis of the AIS, and the corresponding phalloidin-Atto647N intensity was
643 then extracted using Fiji. The F-actin rings are hence represented by the periodical peaks of phalloidin-
644 Atto647N fluorescent signal along the segmented line. The extracted intensity profile was loaded into
645 Peak Cal 3.0 and smoothed over five pixels to filter the background noise. The indices of phalloidin
646 peaks were then detected using python built-in function Find Peaks. The distance was calculated by
647 subtracting the indices between two adjacent peaks and then times 20 nm pixel size.

648 **Microtubule extraction and staining**

649 The staining of tyrosinated and acetylated microtubules (MTs) was performed accordingly to
650 previously described protocol[46]. In short, extra low density neurons (20,000 cells/ml) were grown on
651 18 mm high precision glass coverslips till DIV10. Then neurons were pre-extracted for 1 min using MT-
652 Extraction buffer (0.3% Triton X-100, 0.1% glutaraldehyde, 80 mM PIPES, 1 mM EGTA, 4 mM MgCl2,
653 pH 6.8) and fixed for 10 min using EM grade 4% PFA, 4% sucrose in PBS at 37°C. After 3x wash in PBS,

654 neurons were immunostained with antibodies against tyrosinated and acetylated α-tubulin for
655 dynamic and stable microtubules, respectively. Antibody against TRIM46 was used to locate the AIS.
656 Samples were imaged on an Abberior gatedSTED system as described above. The distribution of stable
657 and dynamic MTs along the width of a region of interest was displayed by extracting and plotting the
658 fluorescent intensities of a 2x2 pixel line along the latitudinal axis.

659 **Imaging of MT dynamics**

660 High density neurons (60,000 cells/ml) were grown on 35 mm glass bottom petri dish and transfected
661 with EB3-Tdtomato plasmid at the age of DIV13 and imaged 12 hours post transfection using spinning
662 disk confocal microscope. Shortly before imaging, conditioned medium was replaced by BrainPhys
663 medium containing neurofascin-CF640R antibody (1:200 dilution) to label the AIS. Dishes were return
664 in the incubator and kept at 37°C with 5% CO2 for 5 min. Afterwards, conditioned medium was
665 exchanged and neurons were return in the incubator for 10 min to recover. AcD and nonAcD neurons
666 were then identified based on neurofascin and EB3-Tdtomato channel. For that images were acquired
667 as z-stacks with 0.7 µm step size, 5% laser power and 100 ms exposure time. Then, EB3 channel of
668 selected neurons was recorded as a time lapse with frame rate of 1.3 s / frame and 5% laser power for
669 5 min.

670 **Axonal and dendritic cargo trafficking assays**

671 For axonal cargo trafficking assay, high density DIV5 neurons (60,000 cells/ml) on 35 mm glass bottom
672 petri dishes were infected for 2 days with rAAV9 virus expressing EGFP-Rab3A. At DIV7, the AIS was
673 labelled at 37°C with 5% CO2 for 5 min by replacing conditioned medium with BrainPhys medium
674 containing neurofascin-CF640R antibody (1:500 dilution). Neurons were then placed back to
675 conditioned medium for recovery. AcD and nonAcD neurons were selected based on EGFP-Rab3A and
676 neurofascin-CF640R fluorescence. Z-stack image was taken for both channels with 0.7 µm step size,
677 5% laser power and 100 ms exposure time to verify neuronal morphology. To analyse the newly

678 delivered EGFP-Rab3A vesicles and to improve the signal to noise ratio, the vesicles residing at the AIS,
679 stem dendrite and regular dendrite were photo-bleached using 405 nm laser with 70% laser power for
680 5 s. New EGFP-Rab3A vesicles travelling through the photo-bleached regions were continuously
681 imaged with 5 frames per second and 10% laser power for 2 minutes.

682 For dendritic cargo trafficking assay, the AIS of high density DIV7 neurons (60,000 cells/ml) grown on
683 35 mm glass bottom petri dishes was labelled as described above. Then, pre-conjugated Transferrin-
684 Alexa568 (1:1000 dilution) was used to label the endogenous Transferrin receptors (TfRs) by incubation
685 for 15 min at 37°C with 5% CO2 in BrainPhys medium. Then neurons were switched back to the
686 conditioned medium for recovery. AcD and nonAcD neurons were selected based on Transferrin-
687 Alexa568 and neurofascin-CF640R channels. Neuronal morphology was confirmed by z-stack imaging
688 (0.7 µm step size, 5% laser power and 50 ms exposure time) of both channels. Trafficking of TfRs in the
689 AIS, stem dendrite, AcD and regular dendrite was recorded with 5 frames per second and 10% laser
690 power for 2 minutes.

691 **Analysis of microtubule dynamics and cargo trafficking assays**

692 Time lapse imaging data for EB3-Tdtomato, EGFP-Rab3 and Transferrin-568 were analysed using Fiji
693 and self-written python scripts KYMOA 6.0 and KA Post Processing 2.0 (https://github.com/HU-Berlin-
694 Optobiology/AIS-project.git). In short, segmented lines were drew on time lapse images at region of
695 interests (ROIs). The segmented line is along the anterograde direction (e.g., cell body to distal axon),
696 and the width of the segmented line covers the width of the ROIs to include majority of the signals.
697 Corresponding kymograph were then generated using Fiji plugin KymoResliceWide. Coordinates of
698 each trajectory on the kymograph were extracted using freehand tool and get-coordinate function in
699 Fiji. Subsequently, the coordinates were further processed in KYMOA 6.0 and KA Post Processing 2.0.
700 For EGFP-Rab3 and Transferrin-568, we defined vesicles having at least one movement, i.e. frame-to-
701 frame change in the y-coordinate, over 5 continuous pixels and frames as mobile vesicles, and the
702 corresponding movement was considered as a run (Figure S2B and S2C). Otherwise, the vesicles were

703 classified as stationary (Figure S2D). Several parameters were then calculated only for mobile vesicles,
704 such as run length, run speed, run duration and net displacement (Figure S2B and S2C). To define the
705 travelling direction of a mobile vesicle, we took advantage of the net displacement. Mobile vesicles
706 having a displacement above zero were classified as anterogradely transported vesicles, however,
707 below zero were classified as retrogradely transported vesicles (Figure S2B and S2C). During active
708 transport, vesicles sometimes shortly pause at one spot for a few seconds. We thus defined pausing
709 behaviour as a mobile vesicle that stalled at the same position for at least 3 frames (Figure S2B and
710 S2C). It is worth noting that we often observed a vesicle repeatedly moving one pixel, stop for one
711 frame and moving for one pixel again (Figure S2B and S2C). Since those vesicles were neither fully
712 stationary nor being actively transported, we specified this type of movement as passive movement.
713 For EB3-Tdtomato, the running and pausing threshold was set to 2 pixels and 2-10 frames respectively.
714 There was no threshold for passive movement because MT plus ends have unidirectional movements.

715 **Induction of rapid and chronic AIS plasticity**

716 Induction of AIS plasticity in dissociated primary neuron cultures was performed following previously
717 published protocols.[14,15] Briefly, high density dissociated primary neurons (60,000 cells/ml) were
718 depolarised by 15 mM KCl to artificially increase neuronal activity, 15 mM NaCl was used as osmolarity
719 control and 1 µM Tetrodoxin (TTX) was used to silence neuronal activity of the entire culture. For rapid
720 plasticity, neurons were treated for 3 hours at DIV12 and then fixed for 10 min at 37°C. For chronic
721 plasticity, neurons were treated from DIV12 to DIV14 for 48 hours then fixed for 10 min at 37°C. Fixed
722 neurons were immunostained with pre-conjugated anti MAP2-Alexa488 and anti AnkG antibody to
723 label dendrites and AIS respectively and imaged using laser scanning confocal microscope. Tile scan
724 images were taken with 1% laser power for both channels and 5 µm depth in z.

725 **Analysis of AIS length and distance from the soma**

726 The length of AIS and its distance to the starting point of axon was measured based on AnkG
727 fluorescent intensity. Maximum projection of confocal z-stack images was used for this analysis. A 3
728 pixel wide segmented line was drew from the beginning of the axon towards the distal end to cover
729 the entire AIS. The florescent intensity of AnkG staining along the segmented line profile was extracted
730 in Fiji and processed by AIS Pack 2.0, a self-written python script (https://github.com/HU-Berlin-
731 Optobiology/AIS-project.git). The AnkG intensity profile was smoothed over 4 µm to filter out
732 background noise and the peak of the intensity profile was detected. To define the start and the end
733 of the AIS, the algorithm iterate through intensity values from the peak to the left and right side until
734 the value is below 40% of the peak value. Consequently, the left edge of the AnkG intensity profile is
735 the start of the AIS and the right edge is the end. Indices of the left and right edge are subtracted to
736 calculate AIS length, and the AIS distance equals to the left edge of AnkG intensity profile.

737 **Immunostaining of inhibitory and excitatory synapses and cisternal organelle**

738 Low density DIV21 neurons (40,000 cells/ml) were fixed for 10 min at 37°C. For inhibitory and
739 excitatory synapse, fixed neurons were stained either with antibody against VGAT and gephyrin for
740 pre- and post-synaptic sites of inhibitory synapse, or with antibody against VGLUT and homer-1 to
741 visualise the pre- and post-synaptic compartments of excitatory synapse. The AIS was stained either
742 with AnkG or TRIM46 antibody depending on antibody species compatibility. MAP2-Alexa488 antibody
743 was used to visualise cell bodies and dendrites. For the CO, the AIS, cell body and dendrite of fixed
744 neurons were stained in the same way as above. The CO was immunostained by antibody against
745 synaptopodin. All samples were imaged using laser scanning confocal microscope, and a tile scan
746 image was taken with 0.5-1% laser power and 5 µm depth in z. The number of synaptopodin puncta as
747 well as number of inhibitory and excitatory synapses were quantified using Fiji. Maximum projection
748 of tile scan images was used for the analysis. Synaptopodin, VGAT, gephyrin, VGLUT and homer-1

749 puncta within the AIS region were counted using multipoint tool and normalised to the length of
750 measured AIS.

751 **Statistical Analysis and Image representation**

752 Statistical analysis was performed on Prism version 7.03 (GraphPad). Data are represented as
753 percentage or as mean ±SEM. Individual channels in multi-colour images are contrasted for better
754 representation, with set minimum and maximum identical if groups need to be compared. No other
755 modifications were done, unless otherwise stated. All analysis was done on raw images.

756 **Key resource table**

REAGENT or RESOURCE	SOURCE	IDENTIFIER
Antibodies		
anti-AnkG (mouse, dillution 1:500)	Neuromab	Cat#N106_36; RRID:AB_2877524
anti- βIV-Spectrin (mouse, dillution 1:200)	Neuromab	Cat#75-377; RRID:AB_2315818
Anti-neurofascin (mouse, , dillution 1:200)	Neuromab	Cat#75-172; RRID:AB_2282826
Anti-TRIM46 (rabbit, dillution 1:500)	Synaptic Systems	Cat#377003 RRID:AB_2631232
Anti-tyrosinated α tubulin (mouse, dillution 1:500)	Synaptic system	Cat# 302 117 RRID:AB_2620047
Anti-acetylated α tubulin (mouse, dillution 1:500)	Santa Cruz	Cat#sc-23950 RRID:AB_628409
anti-MAP2-Alexa Fluor-488 (mouse, dillution 1:500)	Merck Millipore	Cat#MAB3418X; RRID:AB_11212966
Anti-synaptopodin (rabbit, dillution 1:500)	Synaptic Systems	Cat#163002; RRID:AB_887825
Anti-gephyrin (mouse, dillution 1:500)	Synaptic Systems	Cat#147 011 RRID: AB_887717
anti-homer-1 (mouse, dillution 1:500)	Synaptic Systems	Cat#160011; RRID:AB_2120992
anti-VGAT (mouse, dillution 1:500)	Synaptic Systems	Cat# 131011; RRID:AB_887872

anti-VGLUT1 (guinea pig, dillution 1:500)	Synaptic Systems	Cat#135304; RRID:AB_887878
anti-mouse-Alexa Fluor 568 (dillution 1:500)	Thermo Fisher Scientific	Cat#A-11004; RRID:AB_2534072
anti-mouse-Alexa Fluor 647 (dillution 1:500)	Thermo Fisher Scientific	Cat#A-21235; RRID:AB_2535804
anti-rabbit-Alexa Fluor 568 (dillution 1:500)	Thermo Fisher Scientific	Cat#A-11036; RRID:AB_10563566
anti-mouse-Abberior Star 580 (dillution 1:500)	Abberior	Cat#2-0002-005-1; RRID:AB_2620153
anti-guinea pig-Abberior Star 635p (dillution 1:500)	Abberior	Cat# ST635P-1006-500UG; RRID:AB_2893230
Anti-mouse-Nanofluor2X-AbberiorStar635p (dillution 1:500)	Nanotag	Cat#N2002; RRID: N/A
Anti-mouse-Nanofluor2X-AbberiorStar580 (dillution 1:500)	Nanotag	Cat# N2702; RRID: AB_2936181
Anti-mouse-Alexa594 (dillution 1:200)	Thermo Fisher Scientific	Cat# A-11032 RRID: AB_2534091
Recombinant DNA constructs		
CMV-EB3-Tdtomato	Addgene	Cat#50708 RRID: Addgene_50708
EGFP-Rab3A	Addgene	Cat#49542 RRID: Addgene_49542
rAAV-syn-EGFP-Rab3A	Yuhao Han	this study
Bacterial and Virus Strains		

E. coli XL10Gold	Agilent	Cat#200314
rAAV9-syn-EGFP-Rab3A	UKE virus facility	this study
Experimental Models: Organisms/Strains		
Rat: Wistar Unilever	Envigo/UKE animal facility	HsdCpb:WU
Primers & Enzymes		
rAAV9-Syn-EGFP-Rab3A Forward (5'-3'): GACTCAGATCTCGAGCTCAAGCTTTAGGAATGGCATCCGCCACAGACTC	IDT	this study
rAAV9-Syn-EGFP-Rab3A Reverse (5'-3'): GTTGATTATCGATAAGCTCATATGTCAGCAGGCGCAGTCCTGGT	IDT	this study
HindIII	Thermo Fisher Scientific	Cat#ER0501
FastDigest NdeI	Thermo Fisher Scientific	Cat#FD0583
Hibrid DNA Polymerase	Roboklon	Cat#E2950-01
Critical Commercial Assays		
CF®640R Mix-n-Stain™ antibody labelling kit	Biotium	Cat#92245
Cold Fusion Cloning Kit	BioCat	Cat#MC010A-NCC-SBI
Chemicals and ligands		
Phalloidin-atto647N	Sigma-Aldrich	Cat#65906-10NMOL
Lipofectamine 2000	Invitrogen	Cat#11668027
Transferrin-568	Thermo Fisher Scientific	Cat#T23365
Tetrodotoxin	Roth	Cat#6973.1
Sodium Chloride	VWR Chemicals	Cat#27810.364
Potassium Chloride	Roth	Cat#6781.1
ROTI Histofix	Roth	Cat#A146.6

Trypsin (0.25%)	Thermo Fisher Scientific	Cat#25200-056
Poly-l-lysine	Sigma-Aldrich	Cat#P2636
Glutamine	Thermo Fisher Scientific	Cat#25030024
Medium and supplements		
BrainPhys+SM1 Supplement	StemCell	Cat#05790
DMEM	Sigma	Cat#D6429-500ML
FBS	Thermo Fisher Scientific	Cat#A4766801
Pen/Strep	Thermo Fisher Scientific	Cat#15070063
Software and Algorithmus		
(Fiji is just) ImageJ Versions 1.49v & 1.53t		http://fiji.sc/; RRID:SCR_002285
Prism v7.03	GraphPad	https://www.graphpad.com/scientific-software/prism/
Spyder 4.2.5	Pierre Raybaut & Carlos Cordoba	https://www.spyder-ide.org/
Python 3.8.8	Python	https://www.python.org/about/
R 4.3.0	R	https://www.r-project.org/
Peak Cal 3.0	Yuhao Han	https://github.com/HU-Berlin-Optobiology/AIS-project.git
AIS Pack 2.0	Yuhao Han	https://github.com/HU-Berlin-Optobiology/AIS-project.git

KYMOA 6.0	Yuhao Han	https://github.com/HU-Berlin-Optobiology/AIS-project.git
KA Post Processing 2.0	Yuhao Han	https://github.com/HU-Berlin-Optobiology/AIS-project.git

758 **Supplemental Videos**

759 **Video S1.** Differentiation of nonAcD neurons. Related to Figure 1D. White arrowhead indicates
760 the axon. Frame rate of this video is 15 frames/second.

761 **Video S2.** AcD neuron develop AcD via precursor neurite collateralization. Related to Figure
762 1D and S1A. Orange arrowhead indicates the precursor neurite. White arrowhead indicates
763 the axon. Yellow and pink arrowhead indicates the AcD and stem dendrite, respectively. White
764 arrow indicates the AIS. Black arrow indicates the cell body of AcD neuron being recorded.
765 Frame rate of this video is 15 frames/second.

766 **Video S3.** AcD neuron developing axon and AcD via bifurcation of the precursor neurite.
767 Related to Figure S1B. Orange arrowhead indicates the precursor neurite. White arrowhead
768 indicates the axon. Yellow and pink arrowhead indicates the AcD and stem dendrite,
769 respectively. White arrow indicates the AIS. Black arrow indicates the cell body of AcD neuron.
770 Frame rate of this video is 15 frames/second.

771 **Video S4.** AcD neuron developing axon from collateral of the precursor neurite. Related to
772 Figure S1A. Orange arrowhead indicates the precursor neurite. White arrowhead indicates the
773 axon. yellow and pink arrowhead indicates the AcD and stem dendrite, respectively. White
774 arrow indicates the AIS. Black arrow indicates the cell body of AcD neuron. Frame rate of this
775 video is 15 frames/second.

776 **Video S5.** MT orientation in the axon, stem dendrite and AcD of AcD neuron. Related to Figure
777 2A. Black arrow indicates the axon. Pink arrowhead indicates the stem dendrite. Yellow
778 indicates the AcD. Frame rate of this video is 30 frames/second.

779 **Video S6.** MT orientation in the AIS and somatic dendrite of AcD neuron. Related to Figure 2A.
780 Black arrowhead indicates the AIS. Cyan arrowhead indicates the regular somatic dendrite
781 (Regular D). Frame rate of this video is 30 frames/second.

782 **Video S7.** MT orientation in nonAcD neuron. Related to Figure 2A. Black arrow indicates the
783 axon. Black arrowhead indicates the AIS. Cyan arrowhead indicates the regular somatic
784 dendrite (Regular D). Frame rate of this video is 30 frames/second.

785 **Video S8.** EGFP-Rab3A trafficking in AcD neuron. Related to Figure 4. Black arrowhead
786 indicates the AIS. Pink arrowhead indicates the stem dendrite. Cyan arrowhead indicates the
787 regular somatic dendrite (Regular D). Frame rate of this video is 30 frames/second.

788 **Video S9.** EGFP-Rab3A trafficking in nonAcD neuron. Related to Figure 4. Black arrowhead
789 indicates the AIS. Frame rate of this video is 30 frames/second.

790 **Video S10.** TfR trafficking in AcD neuron. Related to Figure 5. Black arrowhead indicates the
791 AIS. Pink arrowhead indicates the stem dendrite. Yellow arrowhead indicates the axon
792 carrying dendrite (AcD). Black arrow indicates the axon. Frame rate of this video is 30
793 frames/second.

794 **Video S11.** TfR trafficking in nonAcD neuron. Related to Figure 5. Black arrowhead indicates
795 the AIS. Cyan arrowhead indicates the regular somatic dendrite (Regular D). Black arrow
796 indicates the axon. Frame rate of this video is 30 frames/second.

797 **References**

798 1. Yogev S, Shen K. Establishing Neuronal Polarity with Environmental and Intrinsic Mechanisms.
799 *Neuron*. 2017;96(3):638-650. doi:10.1016/j.neuron.2017.10.021

800 2. Dotti CG, Sullivan CA, Banker GA. The establishment of polarity by hippocampal neurons in
801 culture. *J Neurosci*. 1988;8(4). doi:10.1523/jneurosci.08-04-01454.1988

802 3. Takano T, Xu C, Funahashi Y, Namba T, Kaibuchi K. Neuronal polarization. *Dev*.
803 2015;142(12):2088-2093. doi:10.1242/dev.114454

804 4. Yau KW, Schätzle P, Tortosa E, et al. Dendrites In vitro and In vivo contain microtubules of
805 opposite polarity and axon formation correlates with uniform plus-end-out microtubule
806 orientation. *J Neurosci*. 2016;36(4):1071-1085. doi:10.1523/JNEUROSCI.2430-15.2016

807 5. Kapitein LC, Hoogenraad CC. Which way to go? Cytoskeletal organization and polarized
808 transport in neurons. *Mol Cell Neurosci*. 2011;46(1):9-20. doi:10.1016/j.mcn.2010.08.015

809 6. Cai D, McEwen DP, Martens JR, Meyhofer E, Verhey KJ. Single molecule imaging reveals
810 differences in microtubule track selection between kinesin motors. *PLoS Biol*. 2009;7(10).
811 doi:10.1371/journal.pbio.1000216

812 7. Nakata T, Hirokawa N. Microtubules provide directional cues for polarized axonal transport
813 through interaction with kinesin motor head. *J Cell Biol*. 2003;162(6):1045-1055.
814 doi:10.1083/jcb.200302175

815 8. Hirokawa N. Kinesin and Dynein Superfamily Proteins and the Mechanism of Organelle
816 Transport. *Science (80-)*. 1998;279(January 1998):519-526.

817 9. Arnold DB, Gallo G. Structure meets function: Actin filaments and myosin motors in the axon.
818 *J Neurochem*. 2014;129(2):213-220. doi:10.1111/jnc.12503

819 10. Balasanyan V, Watanabe K, Dempsey WP, Lewis TL, Trinh LA, Arnold DB. Structure and
820 Function of an Actin-Based Filter in the Proximal Axon. *Cell Rep*. 2017;21(10):2696-2705.
821 doi:10.1016/j.celrep.2017.11.046

822 11. Watanabe K, Al-Bassam S, Miyazaki Y, Wandless TJ, Webster P, Arnold DB. Networks of
823 Polarized Actin Filaments in the Axon Initial Segment Provide a Mechanism for Sorting Axonal
824 and Dendritic Proteins. *Cell Rep*. 2012;2(6):1546-1553. doi:10.1016/j.celrep.2012.11.015

825 12. Al-Bassam S, Xu M, Wandless TJ, Arnold DB. Differential trafficking of transport vesicles
826 contributes to the localization of dendritic proteins. *Cell Rep*. 2012;2(1):89-100.
827 doi:10.1016/j.celrep.2012.05.018

828 13. Leterrier C. The axon initial segment: An updated viewpoint. *J Neurosci*. 2018;38(9):2135-
829 2145. doi:10.1523/JNEUROSCI.1922-17.2018

830 14. Leterrier C, Potier J, Caillol G, Debarnot C, Rueda Boroni F, Dargent B. Nanoscale Architecture
831 of the Axon Initial Segment Reveals an Organized and Robust Scaffold. *Cell Rep*.
832 2015;13(12):2781-2793. doi:10.1016/j.celrep.2015.11.051

833 15. Vassilopoulos S, Gibaud S, Jimenez A, Caillol G, Leterrier C. Ultrastructure of the axonal
834 periodic scaffold reveals a braid-like organization of actin rings. *Nat Commun*. 2019;10(1):1-
835 13. doi:10.1038/s41467-019-13835-6

836 16. Van Beuningen SFB, Will L, Harterink M, et al. TRIM46 Controls Neuronal Polarity and Axon

Specification by Driving the Formation of Parallel Microtubule Arrays. *Neuron*. 2015;88(6):1208-1226. doi:10.1016/j.neuron.2015.11.012

17. Hu W, Tian C, Li T, Yang M, Hou H, Shu Y. Distinct contributions of Nav1.6 and Nav1.2 in action potential initiation and backpropagation. *Nat Neurosci*. 2009;12(8):996-1002. doi:10.1038/nn.2359

18. -Elek Molnfir B, Somogyi ter, Benedeczky -E Molnfir I, Somogyi P. The Cisternal Organelle as a Ca2+-Storing Compartment Associated with GABAergic Synapses in the Axon Initial Segment of Hippocampal Pyramidal Neurones. Vol 101. Springer-Verlag; 1994.

19. Schlüter A, Rossberger S, Dannehl D, et al. Dynamic Regulation of Synaptopodin and the Axon Initial Segment in Retinal Ganglion Cells During Postnatal Development. *Front Cell Neurosci*. 2019;13(July):1-18. doi:10.3389/fncel.2019.00318

20. Konietzny A, González-Gallego J, Bär J, et al. Myosin V regulates synaptopodin clustering and localization in the dendrites of hippocampal neurons. *J Cell Sci*. 2019;132(16). doi:10.1242/jcs.230177

21. Rasband MN. The axon initial segment and the maintenance of neuronal polarity. *Nat Rev Neurosci*. 2010;11(8):552-562. doi:10.1038/nrn2852

22. Evans MD, Dumitrescu AS, Kruijssen DLH, Taylor SE, Grubb MS. Rapid Modulation of Axon Initial Segment Length Influences Repetitive Spike Firing. *Cell Rep*. 2015;13(6):1233-1245. doi:10.1016/j.celrep.2015.09.066

23. Grubb MS, Burrone J. Activity-dependent relocation of the axon initial segment fine-tunes neuronal excitability. *Nature*. 2010;465(7301):1070-1074. doi:10.1038/nature09160

24. Nathanson AJ, Davies PA, Moss SJ. Inhibitory Synapse Formation at the Axon Initial Segment. *Front Mol Neurosci*. 2019;12(November):1-7. doi:10.3389/fnmol.2019.00266

25. Triarhou LC. Axons emanating from dendrites: phylogenetic repercussions with Cajalian hues. *Front Neuroanat*. 2014;8(November):1-5. doi:10.3389/fnana.2014.00133

26. Thome C, Kelly T, Yanez A, et al. Axon-carrying dendrites convey privileged synaptic input in hippocampal neurons. *Neuron*. 2014;83(6):1418-1430. doi:10.1016/j.neuron.2014.08.013

27. Wahle P, Sobierajski E, Gasterstädt I, et al. Neocortical pyramidal neurons with axons emerging from dendrites are frequent in non-primates, but rare in monkey and human. *Elife*. 2022;11:1-25. doi:10.7554/eLife.76101

28. Hodapp A, Kaiser ME, Thome C, et al. Dendritic axon origin enables information gating by perisomatic inhibition in pyramidal neurons. *Science (80-)*. 2022;377(6613):1448-1452. doi:10.1126/science.abj1861

29. Fréal A, Fassier C, Le Bras B, et al. Cooperative Interactions between 480 kDa Ankyrin-G and EB proteins assemble the axon initial segment. *J Neurosci*. 2016;36(16):4421-4433. doi:10.1523/JNEUROSCI.3219-15.2016

30. Witte H, Neukirchen D, Bradke F. Microtubule stabilization specifies initial neuronal polarization. *J Cell Biol*. 2008;180(3):619-632. doi:10.1083/jcb.200707042

31. Lipka J, Kapitein LC, Jaworski J, Hoogenraad CC. Transport To Dendrites. *Embo J*. 2016;1(3):1-17.

877 32. Tas RP, Chazeau A, Cloin BMC, Lambers MLA, Hoogenraad CC, Kapitein LC. Differentiation
878 between Oppositely Oriented Microtubules Controls Polarized Neuronal Transport. *Neuron*.
879 2017;96(6):1264-1271.e5. doi:10.1016/j.neuron.2017.11.018

880 33. Orth CB, Schultz C, Müller CM, Frotscher M, Deller T. Loss of the cisternal organelle in the
881 axon initial segment of cortical neurons in synaptopodin-deficient mice. *J Comp Neurol*.
882 2007;504(5). doi:10.1002/cne.21445

883 34. Cameron PL, Südhof TC, Jahn R, De Camilli P. Colocalization of synaptophysin with transferrin
884 receptors: Implications for synaptic vesicle biogenesis. *J Cell Biol*. 1991;115(1):151-164.
885 doi:10.1083/jcb.115.1.151

886 35. Niwa S, Tanaka Y, Hirokawa N. KIF1Bβ- and KIF1A-mediated axonal transport of presynaptic
887 regulator Rab3 occurs in a GTP-dependent manner through DENN/MADD. *Nat Cell Biol*.
888 2008;10(11):1269-1279. doi:10.1038/ncb1785

889 36. Rienecker KDA, Poston RG, Saha RN. Merits and Limitations of Studying Neuronal
890 Depolarization-Dependent Processes Using Elevated External Potassium. *ASN Neuro*. 2020;12.
891 doi:10.1177/1759091420974807

892 37. Höfflin F, Jack A, Riedel C, et al. Heterogeneity of the axon initial segment in interneurons and
893 pyramidal cells of rodent visual cortex. *Front Cell Neurosci*. 2017;11(November):1-17.
894 doi:10.3389/fncel.2017.00332

895 38. Schelski M, Bradke F. Neuronal polarization: From spatiotemporal signaling to cytoskeletal
896 dynamics. *Mol Cell Neurosci*. 2017;84:11-28. doi:10.1016/j.mcn.2017.03.008

897 39. Tahirovic S, Hellal F, Neukirchen D, et al. Rac1 regulates neuronal polarization through the
898 WAVE complex. *J Neurosci*. 2010;30(20):6930-6943. doi:10.1523/JNEUROSCI.5395-09.2010

899 40. Govek EE, Newey SE, Van Aelst L. The role of the Rho GTPases in neuronal development.
900 *Genes Dev*. 2005;19(1):1-49. doi:10.1101/gad.1256405

901 41. Burute M, Jansen KI, Mihajlovic M, Vermonden T, Kapitein LC. *Local Changes in Microtubule*
902 *Network Mobility Instruct Neuronal Polarization and Axon Specification*. Vol 8.; 2022.
903 https://www.science.org

904 42. Schelski M, Bradke F. Microtubule retrograde flow retains neuronal polarization in a
905 fluctuating state. *Sci Adv*. 2022;8(44):1-20. doi:10.1126/sciadv.abo2336

906 43. Steele-Nicholson LJ, Andrews MR. Axon-Targeting Motifs: Mechanisms and Applications of
907 Enhancing Axonal Localisation of Transmembrane Proteins. *Cells*. 2022;11(6):1-12.
908 doi:10.3390/cells11060937

909 44. Jungenitz T, Bird A, Engelhardt M, Jedlicka P, Schwarzacher SW, Deller T. Structural plasticity
910 of the axon initial segment in rat hippocampal granule cells following high frequency
911 stimulation and LTP induction. *Front Neuroanat*. 2023;17. doi:10.3389/fnana.2023.1125623

912 45. Hamdan H, Lim BC, Torii T, et al. Mapping axon initial segment structure and function by
913 multiplexed proximity biotinylation. *Nat Commun*. 2020;11(1):100. doi:10.1038/s41467-019-
914 13658-5

915 46. Katrukha EA, Jurriens D, Pastene DS, Kapitein LC. Quantitative mapping of dense microtubule
916 arrays in mammalian neurons. *Elife*. 2021;10:1-25. doi:10.7554/eLife.67925

917

Figure 1

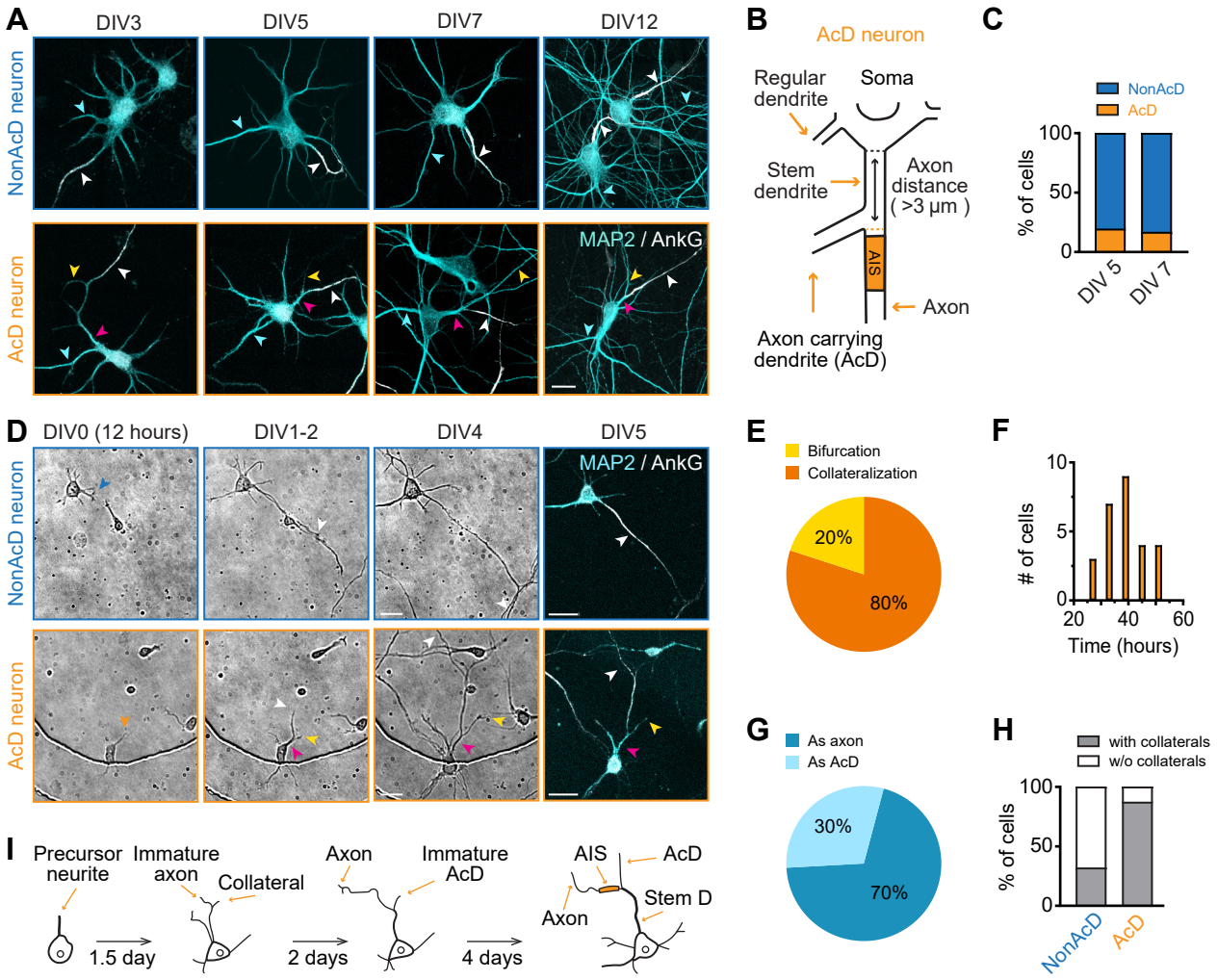
A
DIV3
DIV5
DIV7
DIV12
NonAcD neuron
AcD neuron
MAP2 / AnkG
B
AcD neuron
Regular dendrite
Soma
Stem dendrite
Axon distance (>3 µm)
AIS
Axon
Axon carrying dendrite (AcD)
C
NonAcD
AcD
% of cells
100
50
0
DIV 5
DIV 7
D
DIV0 (12 hours)
DIV1-2
DIV4
DIV5
NonAcD neuron
AcD neuron
MAP2 / AnkG
E
Bifurcation
Collateralization
20%
80%
F
# of cells
10
5
0
20
40
60
Time (hours)
G
As axon
As AcD
30%
70%
H
with collaterals
w/o collaterals
% of cells
100
50
0
NonAcD
AcD
I
Precursor neurite
Immature axon
Collateral
Axon
Immature AcD
AIS
AcD
Stem D
Axon
1.5 day
2 days
4 days

Figure 2

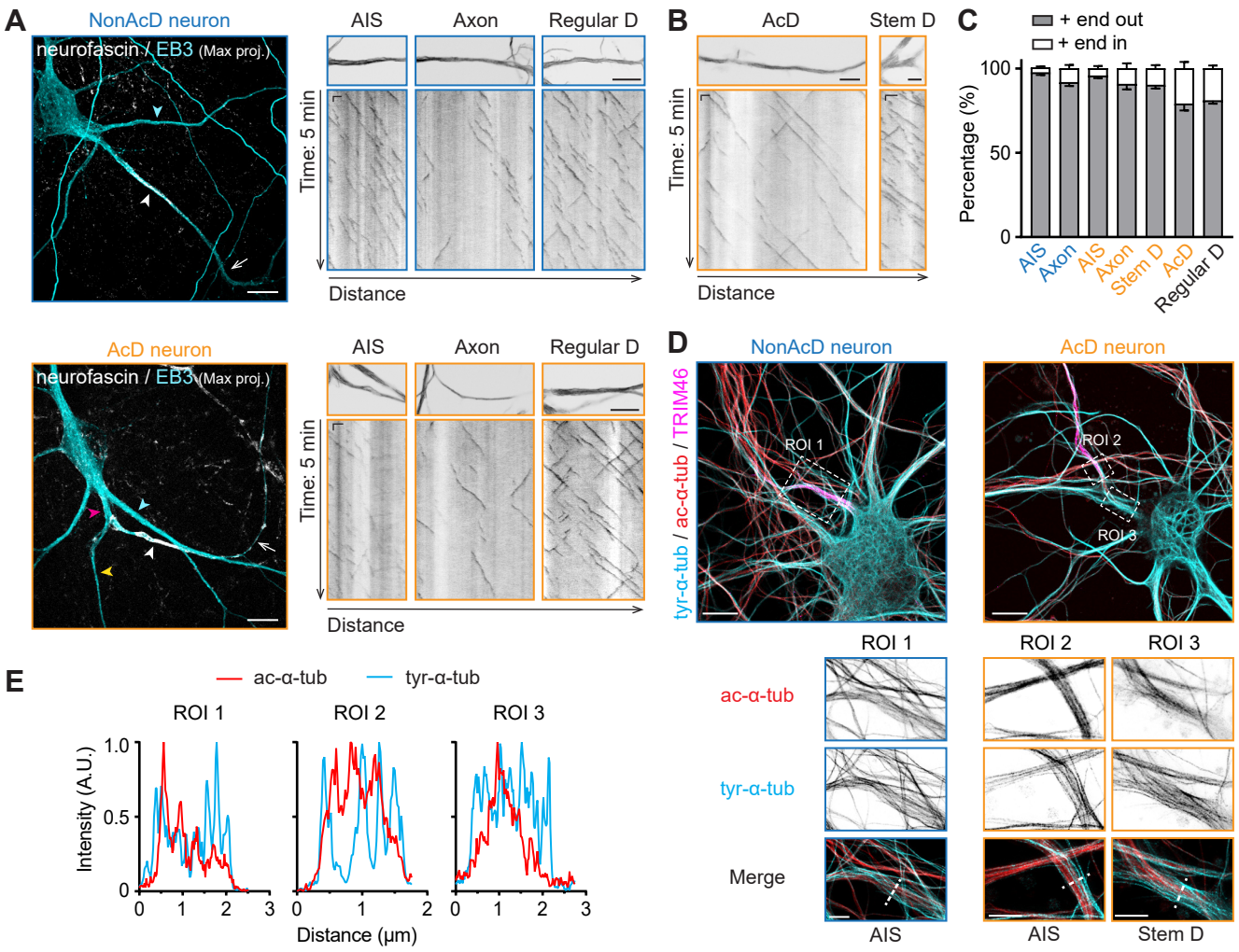
A
NonAcD neuron
neurofascin / EB3 (Max proj.)
AIS
Axon
Regular D
Time: 5 min
Distance
B
AcD
Stem D
Time: 5 min
Distance
C
+ end out
+ end in
Percentage (%)
100
50
0
AIS
Axon
AIS
Axon
Stem D
AcD
Regular D
AcD neuron
neurofascin / EB3 (Max proj.)
AIS
Axon
Regular D
Time: 5 min
Distance
D
NonAcD neuron
AcD neuron
tyr-α-tub / ac-α-tub / TRIM46
ROI 1
ROI 2
ROI 3
ROI 1
ROI 2
ROI 3
ac-α-tub
tyr-α-tub
Merge
AIS
AIS
Stem D
E
ac-α-tub
tyr-α-tub
ROI 1
ROI 2
ROI 3
Intensity (A.U.)
1.0
0.5
0
0
1
2
3
Distance (μm)

Figure 3

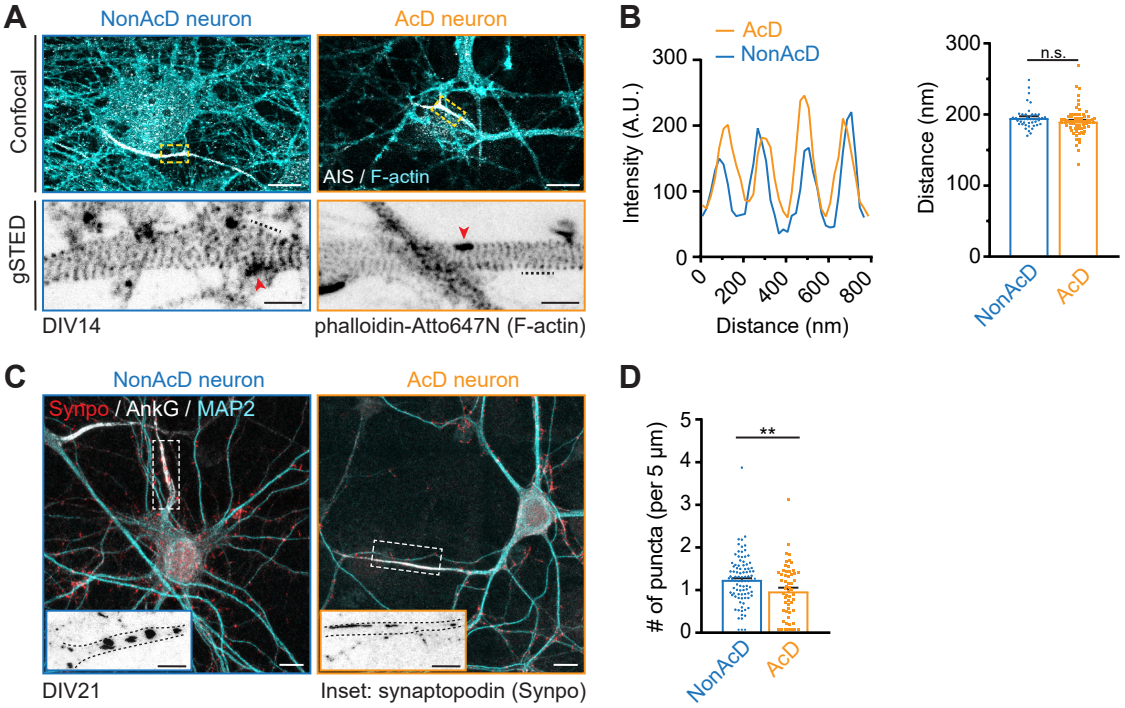
A
NonAcD neuron
AcD neuron
Confocal
gSTED
AIS / F-actin
DIV14
phalloidin-Atto647N (F-actin)
B
AcD
NonAcD
Intensity (A.U.)
Distance (nm)
n.s.
NonAcD
AcD
C
NonAcD neuron
AcD neuron
Synpo / AnkG / MAP2
DIV21
Inset: synaptopodin (Synpo)
D
# of puncta (per 5 µm)
**
NonAcD
AcD

Figure 4

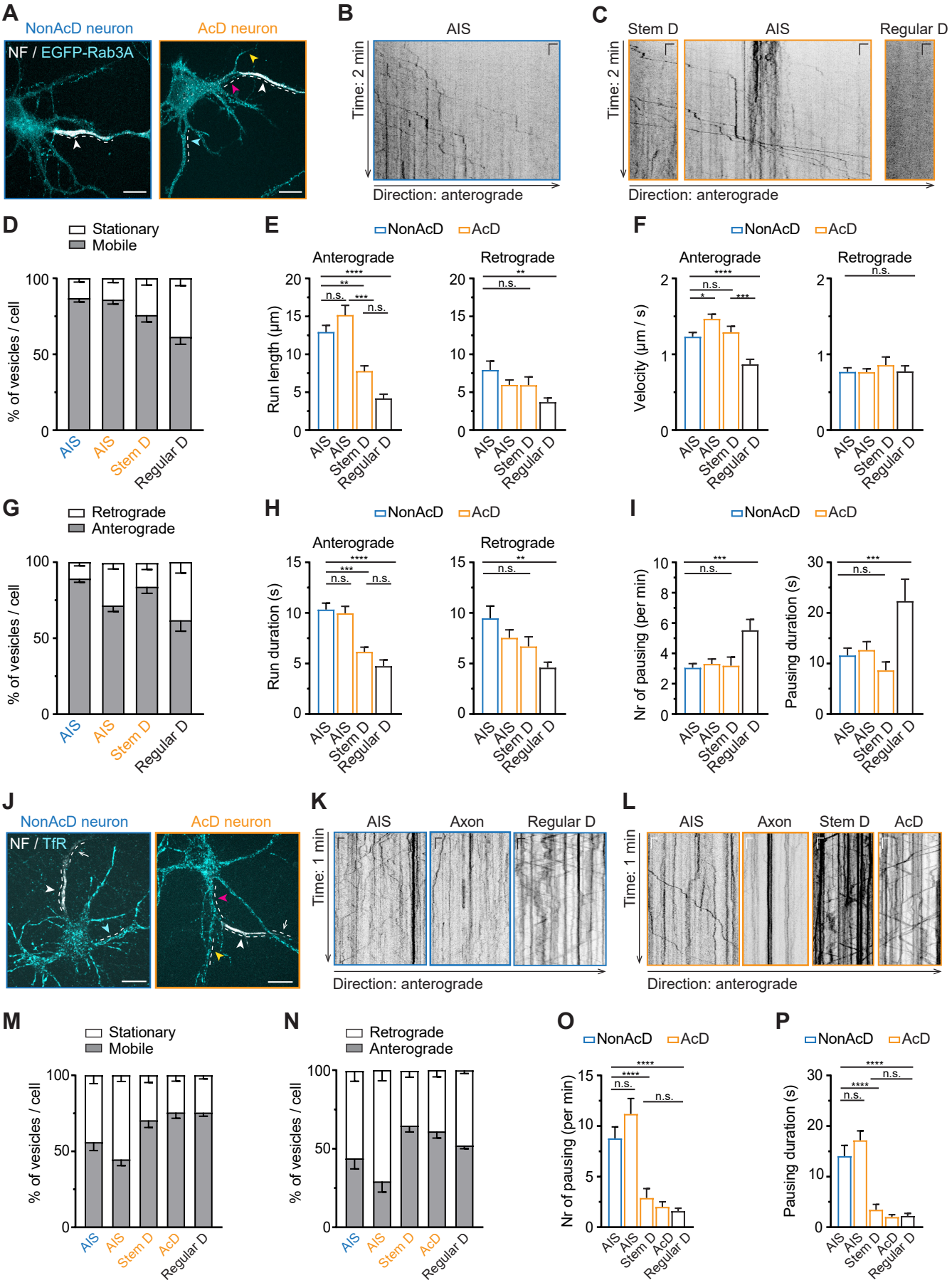
A
NonAcD neuron
AcD neuron
NF / EGFP-Rab3A
B
AIS
Time: 2 min
Direction: anterograde
C
Stem D
AIS
Regular D
Time: 2 min
Direction: anterograde
D
Stationary
Mobile
% of vesicles / cell
AIS
AIS
Stem D
Regular D
E
NonAcD
AcD
Anterograde
Retrograde
Run length (µm)
F
Velocity (µm / s)
G
Retrograde
Anterograde
H
Run duration (s)
I
Nr of pausing (per min)
Pausing duration (s)
J
NonAcD neuron
AcD neuron
NF / TfR
K
AIS
Axon
Regular D
Time: 1 min
Direction: anterograde
L
AIS
Axon
Stem D
AcD
Time: 1 min
Direction: anterograde
M
Stationary
Mobile
% of vesicles / cell
AcD
N
Retrograde
Anterograde
O
Nr of pausing (per min)
P
Pausing duration (s)

Figure 5

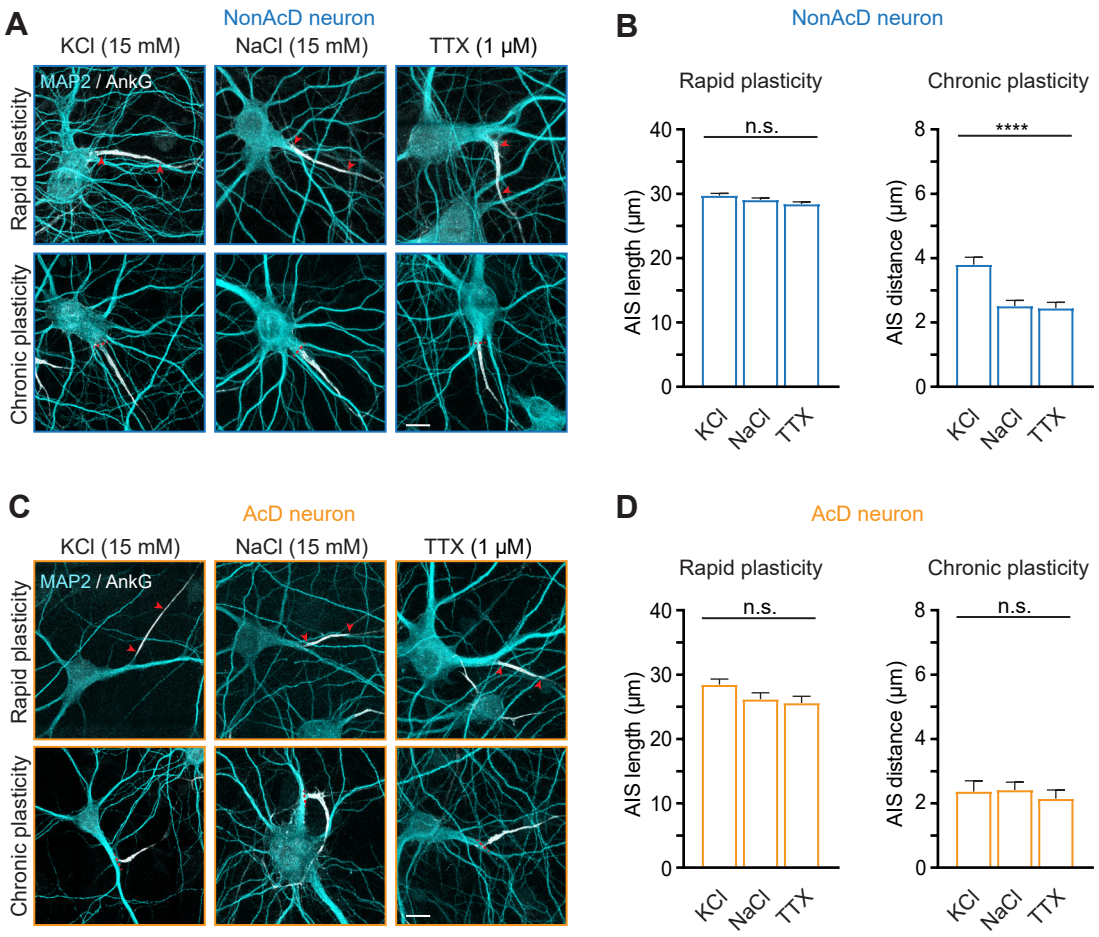
A
NonAcD neuron
KCl (15 mM)
NaCl (15 mM)
TTX (1 μM)
MAP2 / AnkG
Rapid plasticity
Chronic plasticity
B
NonAcD neuron
Rapid plasticity
Chronic plasticity
n.s.
****
AIS length (μm)
AIS distance (μm)
KCl
NaCl
TTX
C
AcD neuron
KCl (15 mM)
NaCl (15 mM)
TTX (1 μM)
MAP2 / AnkG
Rapid plasticity
Chronic plasticity
D
AcD neuron
Rapid plasticity
Chronic plasticity
n.s.
n.s.
AIS length (μm)
AIS distance (μm)
KCl
NaCl
TTX

Figure 6

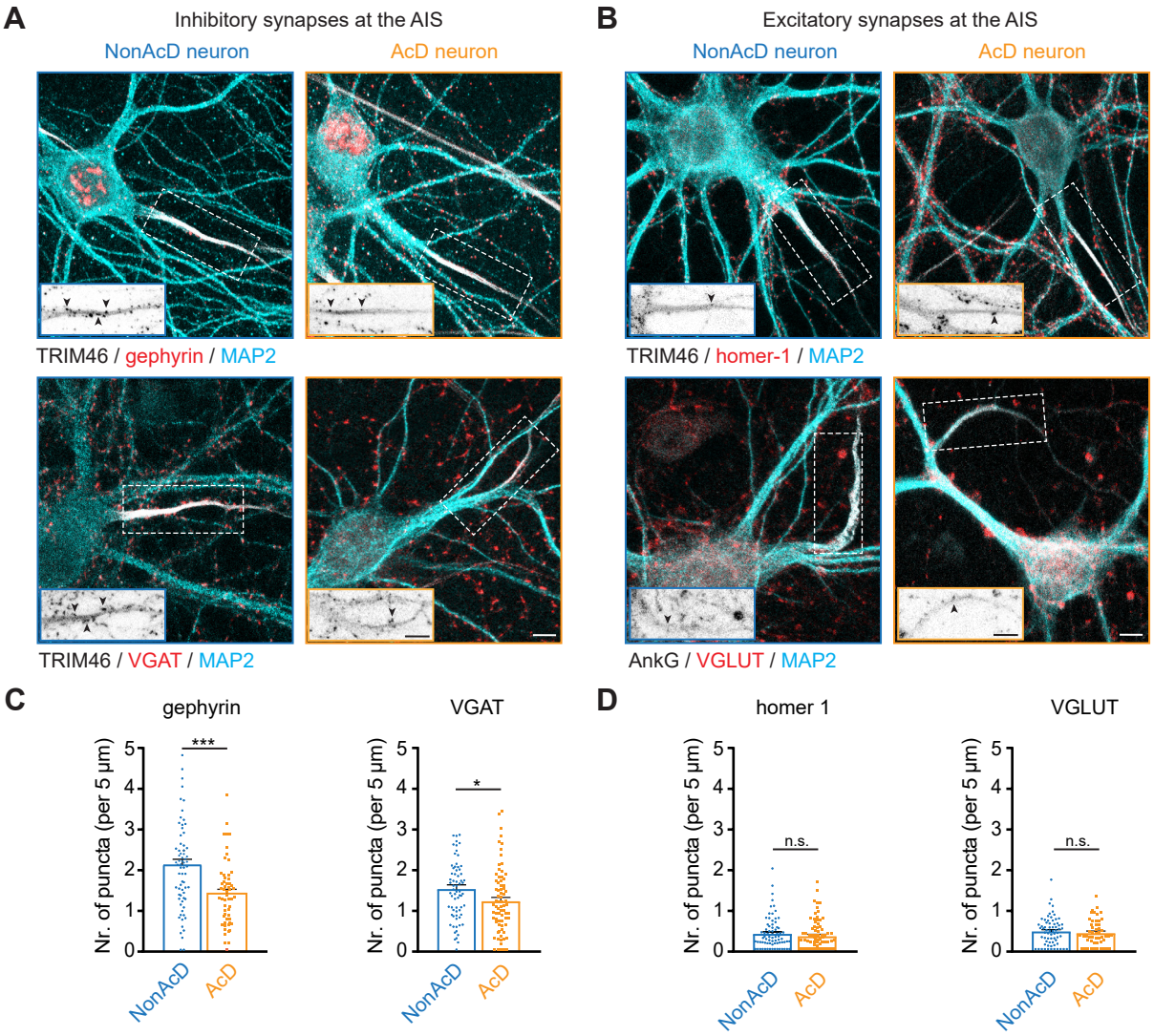
A
Inhibitory synapses at the AIS
NonAcD neuron
AcD neuron
TRIM46 / gephyrin / MAP2
TRIM46 / VGAT / MAP2
B
Excitatory synapses at the AIS
NonAcD neuron
AcD neuron
TRIM46 / homer-1 / MAP2
AnkG / VGLUT / MAP2
C
gephyrin
VGAT
Nr. of puncta (per 5 µm)
***
*
NonAcD
AcD
D
homer 1
VGLUT
n.s.
n.s.